

<b>REPORT DOCUMENTATION PAGE</b>			<b>Form Approved</b> <b>OMB No. 0704-0188</b>	
Public reporting burden for this collection of information is estimated to average 1 hour per response, including the time for reviewing instructions, searching data sources, gathering and maintaining the data needed, and completing and reviewing the collection of information. Send comments regarding this burden estimate or any other aspect of this collection of information, including suggestions for reducing this burden to Washington Headquarters Service, Directorate for Information Operations and Reports, 1215 Jefferson Davis Highway, Suite 1204, Arlington, VA 22202-4302, and to the Office of Management and Budget, Paperwork Reduction Project (0704-0188) Washington, DC 20503.				
<b>PLEASE DO NOT RETURN YOUR FORM TO THE ABOVE ADDRESS.</b>				
<b>1. REPORT DATE (DD-MM-YYYY)</b> 20-12-2010		<b>2. REPORT TYPE</b> Final Performance Report		<b>3. DATES COVERED (From - To)</b> Jul 2007 - Sep 2010
<b>4. TITLE AND SUBTITLE</b> Engineering Photonic Devices and Materials Through Quantum Confinement and Electromagnetic Design			<b>5a. CONTRACT NUMBER</b>	
			<b>5b. GRANT NUMBER</b> FA9550-07-1-0292	
			<b>5c. PROGRAM ELEMENT NUMBER</b>	
<b>6. AUTHOR(S)</b> Prather, Dennis			<b>5d. PROJECT NUMBER</b>	
			<b>5e. TASK NUMBER</b>	
			<b>5f. WORK UNIT NUMBER</b>	
<b>7. PERFORMING ORGANIZATION NAME(S) AND ADDRESS(ES)</b> University of Delaware 210 Hullihen Hall Newark, DE 19716			<b>8. PERFORMING ORGANIZATION REPORT NUMBER</b> ELEG332239-123110	
<b>9. SPONSORING/MONITORING AGENCY NAME(S) AND ADDRESS(ES)</b> Air Force Office of Scientific Research 875 North Randolph Street Arlington, VA 22203-1768			<b>10. SPONSOR/MONITOR'S ACRONYM(S)</b>	
			<b>11. SPONSORING/MONITORING AGENCY REPORT NUMBER</b>	
<b>12. DISTRIBUTION AVAILABILITY STATEMENT</b>  Approved for public release; distribution is unlimited.				
<b>13. SUPPLEMENTARY NOTES</b> None				
<b>14. ABSTRACT</b> In this effort, devices which used quantum confinement for light emission were designed. Two methods of quantum confinement were investigated; Si quantum dots (nanocrystals) and III-V pyramidal quantum dots. Investigation of Si nanocrystals included studies of the effects of varying silicon layer thickness and their agreement with quantum confinement theory. Along with photoluminescence, electroluminescence of silicon nanocrystals films was investigated under both DC and pulsed pumping. A power conversion efficiency of approximately $3 \times 10^{-6}$ was obtained at low current densities for these nanocrystals structures. Microdisk and microgear cavities were made and quality factors were extracted from these devices. An alternative approach to MBE growth of AlGaAs quantum dots was taken in this work. The fabrication approach that was used was to grow complete layers with MBE processing and then selectively etch the structures. Pyramid type structures were created in these materials with a combination of wet and dry etch techniques. The effects of the concentration of Al on the AlGaAs on etch rates and selectivity were investigated as a key part of the project. The process was refined to be able to create high density quantum confinement structures.				
<b>15. SUBJECT TERMS</b> Quantum dots, nanocrystals, microdisk, si source,				
<b>16. SECURITY CLASSIFICATION OF:</b>		<b>17. LIMITATION OF ABSTRACT</b> UU	<b>18. NUMBER OF PAGES</b> 38	<b>19a. NAME OF RESPONSIBLE PERSON</b> Dennis Prather
a. REPORT U	b. ABSTRACT U			c. THIS PAGE U

# 1

## Cover Sheet

**Project Title:** Engineering Photonic Devices and Materials through Quantum Confinement and Electromagnetic Design

**Contract Number:** FA9550-07-1-0292

### Performing Organization

University of Delaware  
Electrical and Computer Engineering Department  
140 Evans Hall;  
Newark, DE 19716

**Principal Investigator:** Dr. Dennis Prather

**Dates Covered:** 1 July 2007 to 30 September 2010

## 2 Objectives

Our broad objective is to realize photonic devices with enhanced performance due to the incorporation of carefully designed quantum confined materials. We focused on two quantum confined materials, III-V pyramidal quantum dots for enhanced linear electro-optic effects and Si quantum dots (called nanocrystals) for enhanced light emission. Our efforts to develop these materials and incorporate them in photonic devices with improved performance can be divided into the following categories.

1. Apply quantum mechanics level modeling to understand the enhanced properties in quantum confined materials and guide the material optimization.
2. Develop a device level modeling tool which accounts for the quantum mechanics based enhanced material properties such that device performance may be used as a design metric in material optimization.
3. Develop and optimize the quantum confined material fabrication processes and perform associated material characterization required to accurately model the device level behavior.
4. Apply the modeling tool to design active photonic devices with enhanced performance owing to the incorporation of novel quantum confined materials.
5. Experimentally fabricate and characterize active photonic devices based on our modeling designs.

## 3 Status of Report

During this project, we investigated quantum confined materials for incorporation in active photonic devices for enhanced device-level performance. This work can be divided into four categories: (1) Quantum mechanics level modeling for optimization of the nanoscale quantum confined material geometry. (2) Device level modeling to understand and guide the incorporation of novel quantum confined materials in photonic devices. (3) Experimental development and characterization of quantum confined materials. (4) Experimental fabrication and testing of photonic devices with integrated quantum confined materials.

In this work, we investigated two quantum confined material systems for two separate applications. The first material system was Si nanocrystals (Si-ncs) which exhibit enhanced light emission relative to bulk Si. The Si-nc material system was studied for the purpose of developing Si compatible light sources, a crucial component in Si photonics. The second material system was III-V pyramidal quantum dots which exhibit an enhanced linear electro-optic effect relative to bulk III-Vs. The III-V quantum dots offer the potential for highly sensitive and efficient electro-optic modulators which could integrate with other III-V photonic devices.

In our efforts to develop a Si-nc based light source, we first developed a device level modeling tool. A great deal of research has been conducted characterizing the luminescence and optical gain properties of Si-nc films; however, relatively few devices have been fabricated which take advantage of the unique properties of this material. We therefore developed a device level modeling tool which accounted for the unique gain and emission behavior of a quantum confined material through a set of rate equations. This method allowed us to study the effects of the specific material emission parameters on device level performance metrics such as enhanced spontaneous emission, amplification and lasing. We then applied this tool to design a series of light emitting devices based on the Si nanocrystal material platform.

Experimentally, we developed and optimized a Si-nc fabrication process. We also conducted extensive analysis of the Si-nc electroluminescence (EL), carrier injection and electrical pumping scheme to realize the most efficient light emitting device (LED) possible. Material characterization allowed us to acquire the parameters governing the emission behavior in our device level modeling tool. Finally, we incorporated the Si-nc material in a series of active photonic devices based on our modeling designs.

Our investigations of III-V quantum dots began by using a quantum mechanics level modeling, *ab initio* modeling tool to understand the source of the enhanced linear electro-optic effect in pyramidal III-V quantum dots. Based on this analysis we were able to identify an optimal nanoscale geometry. We then proposed a method to achieve nanoscale control of the geometry of the quantum dots and experimentally demonstrated the viability of this fabrication technique.

In this report, we begin by presenting the fabrication and characterization of the Si-nc material system and noting the parameters which we used in our modeling. We then present our device-level modeling tool which uses the experimentally measured Si-nc parameters. This modeling tool was used to study a series of Si-nc based light emitting devices. Experimental devices based on some of these designs are presented at the end of the Si-nc section. We then present our simulations of the electro-optic effect in III-V quantum dots and our proposed fabrication process.

## 4 Accomplishments

Quantum confined materials have the potential to provide enhanced functionality in an integrated photonics system. Not only do quantum confined materials offer some excellent and unique material properties, but these materials are generally still compatible with their bulk counterparts. This provides for the opportunity to integrate devices which exhibit enhanced performance due to quantum confinement with other photonic devices on a single substrate. One prominent example of this advantage is III-V quantum wells which have proven to be instrumental in the development of efficient lasers. These quantum wells are compatible with other III-V devices and are therefore amenable to integrated photonics. In this work, we will investigate quantum confined Si and InGaAs based materials. Si nanocrystals (effective quantum dots) exhibit enhanced light emission relative to bulk Si and could prove crucial to the development of a Si based light source capable of integration with existing Si photonic devices. Pyramidal InGaAs quantum dots exhibit stronger linear electro-optic effects relative to bulk III-V crystals, potentially leading to high sensitive and efficient modulators. The remainder of this report will focus on our work with these two materials.

## 4.1 Quantum confinement for enhanced Si-based light emission

Si photonics has the potential to overcome the interconnect bottleneck currently limiting electronic integrated circuit performance. Optical interconnects offer improved bandwidth and reduced power consumption relative to electrical interconnects and the realization of Si compatible optical interconnects would enable monolithic integration with existing complementary metal-oxide-semiconductor (CMOS) processes. This application has driven extensive research in Si photonics and led to the development of a host of Si compatible photonic devices capable of modulation, filtering and detection. The main component lacking from the Si photonics toolkit is an electrically pumped light source. One of the most promising approaches to developing such a light source is quantum confined Si which mitigates the effects of the indirect bandgap which prohibits efficient light emission in bulk Si. In this work, we investigated Si quantum dots (called nanocrystals) in an SiO<sub>2</sub> host. This material system has demonstrated EL, stimulated emission and optical gain.

In our efforts to develop a Si-nc based light source, we developed and optimized a material fabrication process and performed extensive material characterization. We investigated EL in our Si-nc films, modeled the current transport mechanism, and developed a pulsed excitation scheme to improve the device efficiency. We then developed a device level modeling tool which accounted for the unique gain and emission properties of our Si-nc film. We used this modeling tool to design a series of Si-nc based devices. Finally, we fabricated and characterized several Si-nc devices based on our modeling.

### 4.1.1 Si nanocrystal material optimization

Si-nc films were fabricated by depositing a superlattice consisting of alternating thin layers of a-Si and SiO<sub>2</sub> via plasma-enhanced chemical vapor deposition (PECVD). The a-Si layers were deposited in a SiH<sub>4</sub> and Ar environment while the SiO<sub>2</sub> layers were deposited in a SiH<sub>4</sub> and N<sub>2</sub>O environment. The a-Si layers were ~1.5 nm thick and the SiO<sub>2</sub> layers were ~2 nm thick. After deposition, the films were annealed in a N<sub>2</sub> environment at 1100 °C for one hour. This annealing process served to precipitate nanocrystal formations in the a-Si layers. We performed transmission electron microscopy (TEM) on the post annealed Si-nc film, as shown in Fig. 1. Crystalline formations are clearly evident in the a-Si layer, although the entire a-Si layer does not appear to be crystalline. As a result, we do not consider the film to be composed of Si quantum wells, despite the superlattice structure. Rather, the superlattice approach provides us with an intuitive ability to constrain the size of the silicon nanocrystals by limiting the thickness of the a-Si layer.

The emission wavelength in Si-ncs corresponds to the energy of the Si-nc bandgap, which in turn depends on the nanocrystal size. A simple relationship describes the dependence of the nanocrystal bandgap,  $E_g$ , on its diameter,  $d$ :  $E_g \sim d^{-1.5}$  [1]. In accordance with this trend, we expected that by changes in the thickness of the a-Si layer would manifest as a shift in the emission wavelength due to the change in the size of the nanocrystals in the film. Specifically, as the a-Si layer thickness was reduced, we expected the emission wavelength to blue shift. To confirm this expectation, we collected photoluminescence (PL) from Si-nc films with three

different a-Si layer thicknesses: 0.8 nm, 1.0 nm and 1.2 nm. The SiO<sub>2</sub> layers were 2 nm in each case and the structure consisted of ten periods. PL was measured by exciting the Si-nc film with a focused 532 nm laser from above. Emission was collected from above using an off-axis parabolic mirror focused to the entrance slit of a spectrometer. The PL signal, shown in Fig. 1(b), was collected at room temperature and corrected for the response of the system. We observed typical Si-nc PL in the visible spectrum with a linewidth of ~150 nm. We also observed that the peak wavelength blue shifted for Si-nc films with thinner a-Si layers, as expected.

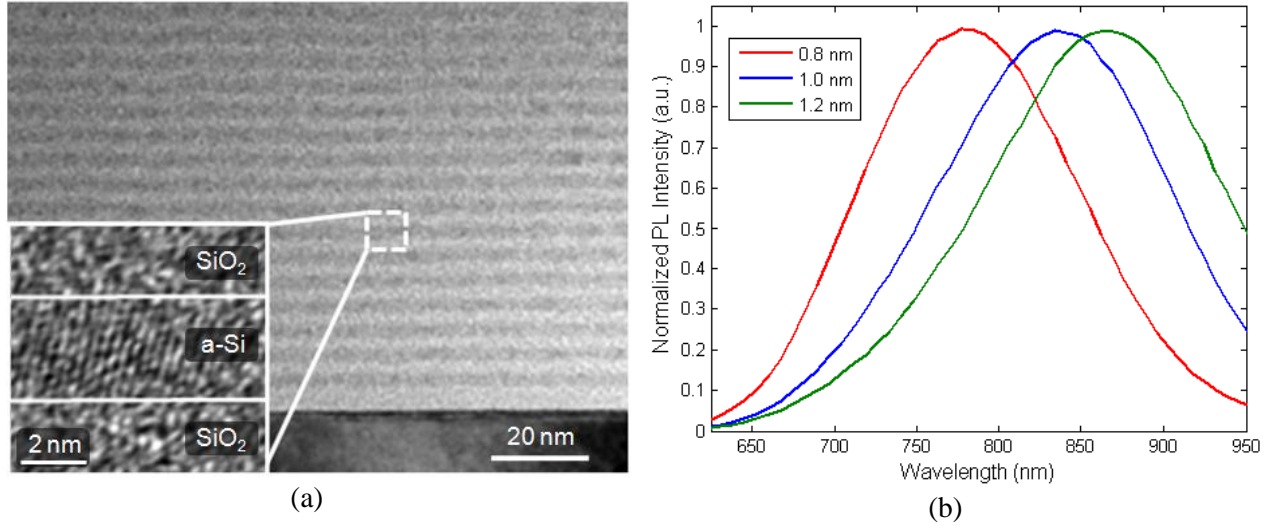


**Figure 1.** (a) Cross sectional TEM image of the Si-nc film. The a-Si/SiO<sub>2</sub> superlattice structure is clearly evident. The inset shows crystalline formations in the a-Si layer. (b) PL spectra for Si-nc films with varying a-Si layer thickness, as indicated in the legend. As the a-Si layer thickness increases, so does the size of the post-anneal nanocrystals, and the subsequent luminescence in red shifted due to a reduction in quantum confinement. After [2].

Aside from the luminescence properties of the Si-nc films, another parameter required to accurately model Si-nc based devices is the refractive index. In order to characterize the refractive index and loss in our Si-nc films, we performed spectroscopic ellipsometry. We used a Tauc-Lorentz model to fit the Si-nc material behavior and extracted the real and imaginary parts of the refractive index as a function of wavelength, as shown in Fig. 2. We observed that the real part of the index is ~1.72 in the Si-nc luminescence region and reduces only slightly in the telecommunication region around 1550 nm. The imaginary part of the refractive index, corresponding to the material loss, is too small to be detected by ellipsometry. We therefore used the Bruggeman effective medium approximation to calculate the loss at 800 nm by considering the film to be a combination of 25% Si, with an effective index of  $3.73+0.009i$ , and 75% SiO<sub>2</sub>, with an effective index of 1.454 at 800 nm [3]. Using this method we found the imaginary component of the refractive index,  $k$ , to be .0014.

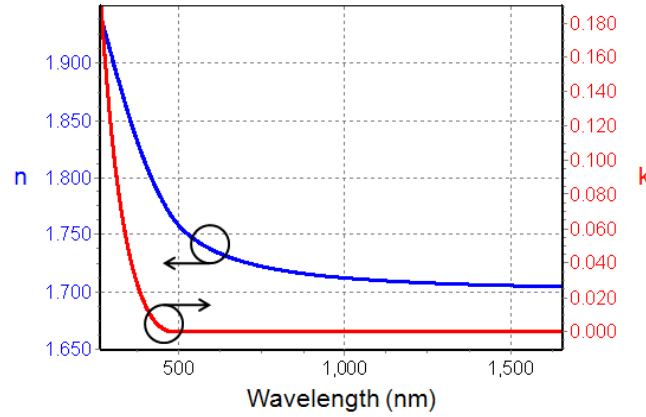


**Figure 2.** Real and imaginary part of the refractive index for the Si-nc film as determined by ellipsometry using a Tauc-Lorentz model.

#### 4.1.2 Si nanocrystal electroluminescence

While the PL is an important metric in optimizing the Si-nc material, electrical excitation is crucial for many integrated devices. We therefore investigated current transport and EL in the optimized Si-nc films. In order to collect EL, we deposited Si-nc films consisting of 30 periods of a-Si and SiO<sub>2</sub> (approximately 100 nm total thickness) on a p-type Si substrate. We then deposited circular indium tin oxide (ITO) contacts with a diameter of 1 mm. Conventional photolithography, followed by liftoff in acetone was used to pattern the ITO circles. The ITO contact was 100 nm thick and optimized for conductivity and transparency. The optimized film had a resistivity of  $\sim 75 \text{ } \Omega/\text{square}$  and a loss coefficient of  $\sim 1000 \text{ cm}^{-1}$ . The sample was placed on a copper sheet so that we could probe the substrate by contacting the copper. We then collected EL by probing the copper and the ITO contact with tungsten probe tips and applying a positive voltage to the ITO contact. The normalized EL spectra for the three Si-nc devices with varying a-Si layer thicknesses are presented in Fig. 3. We observe a similar shift in the peak of the EL spectra as in the PL. Based on this trend, we conclude that the EL emission has the same origins as the PL; although the EL spectra are considerably broader than the PL. This broadening indicates that a slightly different distribution of nanocrystals are excited electrically.

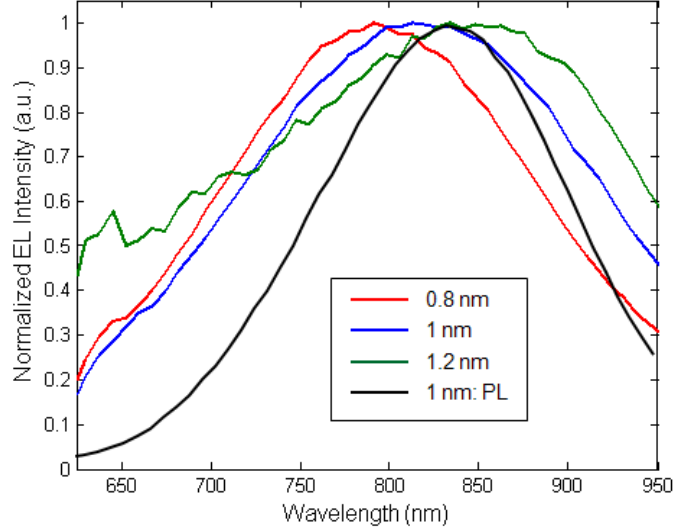


**Figure 3.** EL collected from Si-nc films with varying a-Si layer thickness (indicated in the legend). We observe a similar blue shift in peak luminescence as in the PL spectra. We also note that the EL spectra are somewhat broader than the PL spectrum (indicated in black). After [2].

Aside from measuring EL, we also investigated the current transport mechanism which is an important factor in determining the efficiency and stability of electrically pumped Si-nc devices. The transport mechanism in a-Si/SiO<sub>2</sub> devices is most commonly attributed to either Frenkel-Poole (FP) emission [4] or Fowler-Nordheim (FN) conduction [5]. In our analysis of electrical conduction we therefore compared the experimental results to both models. FP emission relies on the thermal emission of trapped carriers from within a barrier. Within this model, the current density  $J$  is described as a function of the electric field  $E$  by the equation [6]:

$$J = A \cdot E e^{-\frac{1}{kT} \left( q\phi_B - \sqrt{\frac{q^3}{\pi\epsilon}} \cdot \sqrt{E} \right)} \quad (1)$$

where  $A$  is a proportionality constant,  $q$  is the elementary charge,  $T$  is the temperature,  $\phi_B$  is the barrier height,  $k$  is Boltzmann's constant, and  $\epsilon$  is the permittivity of the Si-nc material. The current density of the p-i-ITO devices measured in reverse bias is presented on an FP plot in Fig. 4(a). The linear region between 1500 and 2500 (V/cm)<sup>1/2</sup> indicates that FP emission may be occurring; this range corresponds to an electric field of 2-5 MV/cm. Intuitively, this is understood in terms of the nanocrystals acting as carrier traps between the oxide layers of the superlattice in accordance with FP phenomenology.

While FP emission fits well and provides an intuitive explanation for conduction, we also considered FN conduction, which results from tunneling that occurs at high electric fields. In the FN model, the current density  $J$  is described as a function of the electric field  $E$  by the equation [7]:

$$J = A \cdot \frac{q^2 E^2}{\pi^2 \hbar \phi} \cdot e^{\left( \frac{-C \sqrt{m^*} (q\phi)^{3/2}}{\hbar q E} \right)} \quad (2)$$

where  $A$  and  $C$  are free parameters of the model,  $q$  is the elementary charge,  $\hbar$  is Planck's constant,  $\phi$  is the barrier height, and  $m^*$  is the effective mass of an electron. The current density of the p-i-ITO devices measured in reverse bias is plotted on an FN plot in Fig. 4(b). The plot

exhibits a linear relationship between 0.2 and 0.5 cm/MV, which corresponds to an electric field of 2-5 MV/cm, indicating that FN tunneling may also contribute to the current transport.

Thus, both Frenkel-Poole and Fowler-Nordheim theories for current transport fit the experimental data over the same range of electric field. Based on these results alone, it is not possible to conclude that one of the mechanisms is solely responsible for the conduction in the p-i-ITO devices. In addition, previous researchers have concluded that more than one mechanism can contribute to conduction in silicon nanocrystal devices [8], thus it is possible that both FP and FN conduction are present in our devices.

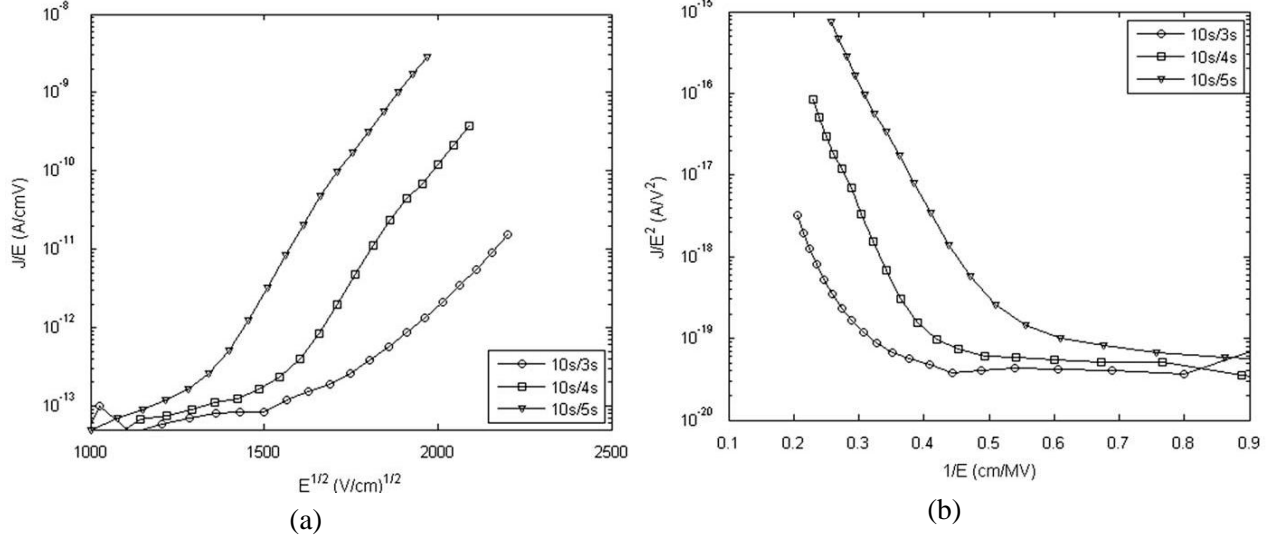


**Figure 4.** (a) FP plot of current mechanism in Si-nc devices. (b) FN plot of the current mechanism in the same devices. The experimental data on both plots follows a linear relationship indicating that both FP and FN current transport mechanisms are present in our devices. After [2].

To determine whether FP or FN is the dominant current mechanism we can investigate the temperature dependence of the current-voltage relationship. As the equations presented above reveal, FP based conduction has temperature dependence while FN tunneling

does not. If FP conduction dominates, then at electric fields where  $q\phi_B > \sqrt{\frac{q^3}{\pi\epsilon}} \cdot \sqrt{E}$ , the current density should increase when temperature increases. Intuitively, the FP mechanism is based on thermal excitation of carriers out of traps; therefore, at a given electric field, we should expect more carriers to escape traps as the temperature increases [6]. Fig. 5 shows an FP plot of the current-voltage relationship for a range of temperatures between 298 and 372 Kelvin. Clearly, the increase in temperature resulted in an increase in the current density, and furthermore, the relationship remains linear on the FP plot for all of the temperatures. Since FN tunneling is not expected to exhibit temperature dependence, these results indicate that FP emission is the dominant conduction mechanism in our Si-nc LEDs.

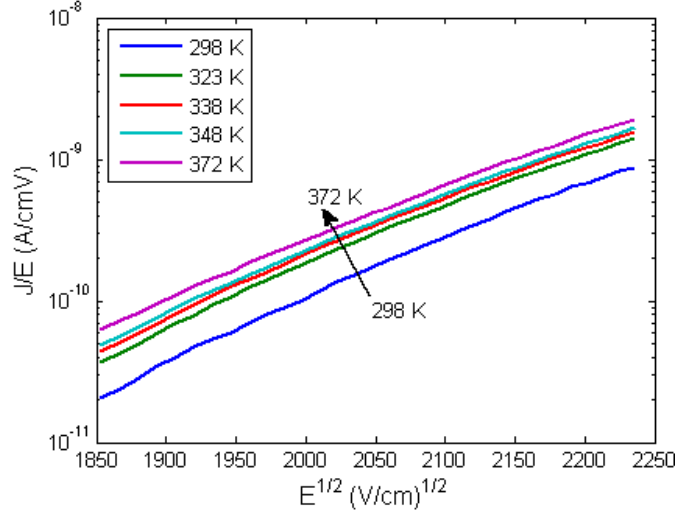


**Figure 5.** Temperature dependent FP plot. The increase in current with temperature indicates that FP is the dominant current transport mechanism.

Our investigations of EL in Si-nc devices presented thus far were performed by applying a DC signal. Unfortunately, due to the insulating nature of the Si-nc films, strong electric field and high voltages are required to inject sufficient current to measure EL under a DC bias. Furthermore, light emission under DC excitation is typically associated with an impact excitation process, which can cause damage to the insulating material resulting in devices that are inefficient and unstable. Recently, researchers have found that more efficient and stable luminescence can be realized via bipolar injection using an alternating voltage [9, 10]. This type of electrical pumping also allows the devices to be driven at voltages much lower than necessary under DC pumping. We therefore investigated the effects of pumping our Si-nc devices using an alternating voltage.

When probing the devices, forward bias was achieved by applying a positive voltage to the substrate and reverse bias was achieved by applying a positive voltage to the ITO. An Agilent 33220A function generator and a Tegam 2340 high voltage amplifier were used to apply square wave biases ranging from 30 V to 80 V peak-to-peak.

For optical power measurements, a two-lens system with a numerical aperture of 0.5 was positioned above the devices to collect the emission. The emission was then detected with a model 818 SL silicon detector head connected to a Newport model 1830-C optical power detector.

In Fig. 6(a), we present the time-resolved voltage and EL signals. In this case we applied an alternating bias of  $\pm 20$  V at 1 kHz. Note that under a DC bias of either positive or negative 20 V, we not observe any EL. However, under alternating bias, as seen in the figure, a spike in the EL occurs at each voltage transition of the applied square wave. The observed behavior can be explained as follows [11]: The forward bias portion of the applied voltage drives the device into accumulation such that holes are injected into the nanocrystals. When the voltage switches to reverse bias, the device is driven into inversion, and electrons are injected. Hence, during the forward-to-reverse transition, electrons are injected into hole-charged nanocrystals, and the opposite occurs during a reverse-to-forward transition. Each of the transitions results in a spike in the EL signal as carriers recombine radiatively inside the nanocrystals. After the initial spike, the nanocrystals continue to accumulate charge in preparation for the next voltage switch. We found the decay time of the EL pulses to be  $\sim 50$   $\mu$ s. Also, the peak of the EL signal after

forward-to-reverse transitions was consistently higher than the peak after reverse-to-forward transitions. Walters, et al. suggest that this occurs due to a difference in the tunneling times of electrons and holes [10].

In order to verify that a bipolar effect is occurring (as opposed to injection of a single carrier type which results in luminescence), we reduced one side of the applied voltage to zero while continuing to monitor the time-resolved EL signal. Fig. 6(b) shows that as either the reverse bias side of the applied voltage was reduced to zero, the EL signal diminished. The same trend was observed when we reduced the forward bias side of the applied voltage. We observed that for electric fields below 6 MV/cm (30 volts for these devices), there was no measurable EL without a bipolar voltage transition. Bipolar injection thus allows us to generate EL at much lower voltages, which helps reduce damage to the material from impact excitation processes and improve reliability.

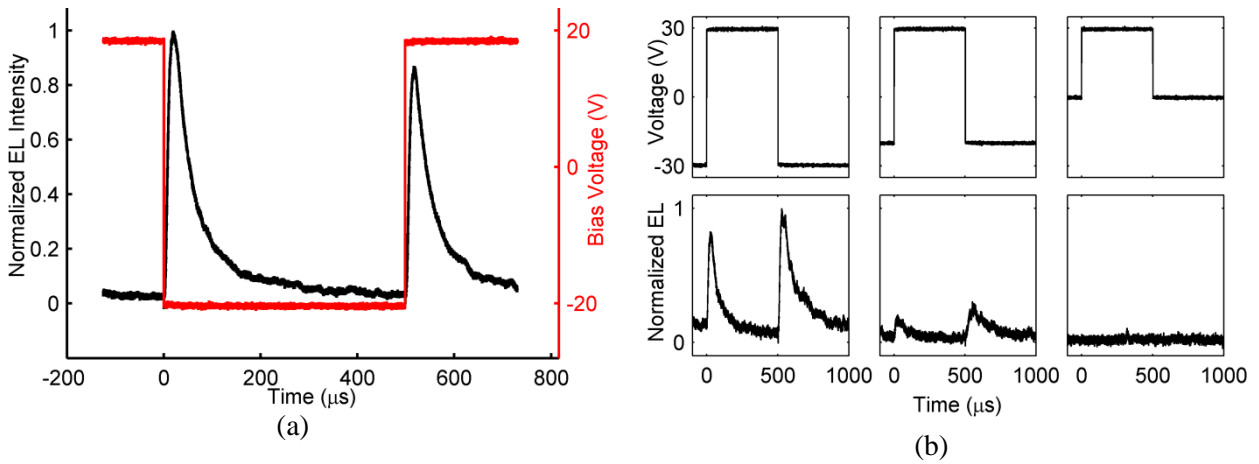


**Figure 6.** (a) A 40 V peak to peak alternating bias was applied at 1 kHz, as shown in red. At each voltage transition we observed a spike in the EL, as shown in black. (b) The EL spikes were only observed under alternating positive and negative bias. In this case we observed a reduction in the EL spikes when the reverse bias voltage was reduced and zero EL when the reverse bias was set to zero. After [12].

Based on the time-dependent behavior observed in Fig. 6, we can consider optimizing the integrated EL output by increasing the driving frequency of the device. For low frequencies, we would expect a doubling of the driving frequency to result in a doubling of the integrated EL output simply because we should double the number of EL spikes per unit time. This behavior should continue until reaching an optimal frequency at which a half-period of the driving voltage is comparable to the decay time of the device. Beyond this frequency we would expect the integrated EL to saturate. Based on these assumptions, we would expect the optimal driving frequency to be 10 kHz, due to the observed 50  $\mu$ s decay. Figure 7(a) shows the integrated EL output as a function of frequency, which we measured by integrating all EL pulses during a fixed period of time while changing the frequency of the driving voltage. At low frequencies (2 – 1000 Hz), the integrated EL signal does not follow the expected scaling behavior. Instead, the integrated EL increases as the square root of frequency. Additionally, the optimal frequency is found to be close to 50 kHz, which is faster than expected.

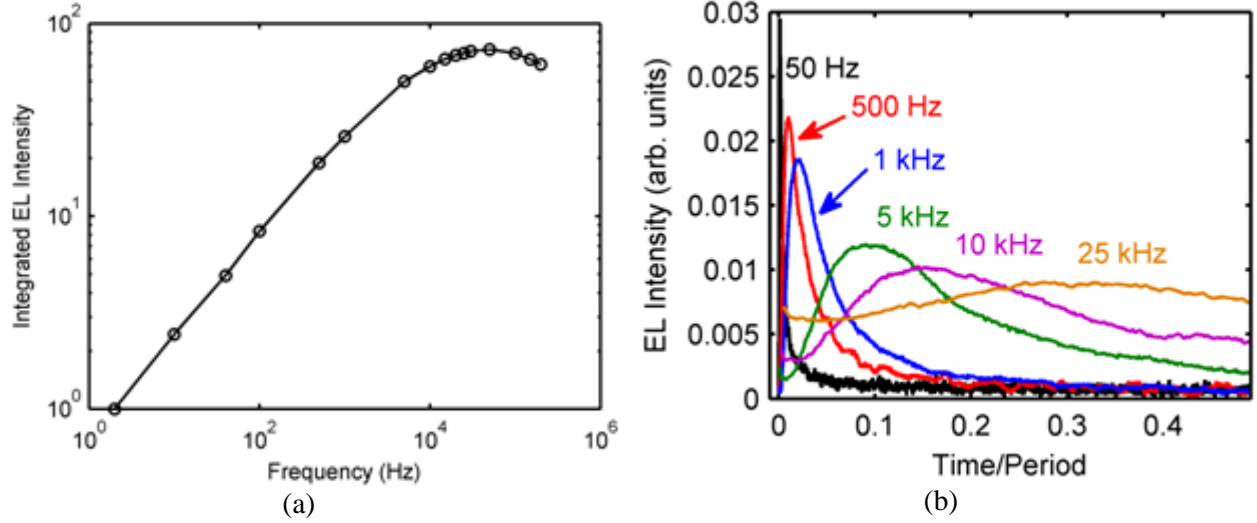


**Figure 7.** (a) The EL integrated over 1 s increases with frequency up to 50 kHz at which point the EL saturates and begins to decline. The EL in each case is normalized to the integrated EL at 2 Hz. (b) Time resolved EL during one half period pulse. After [12].

In order to understand the frequency-dependent behavior observed in Fig. 4, we measured the time-resolved EL signal over one period of the supply voltage for frequencies between 50 Hz and 25 kHz. Fig. 7(b) only shows the results for EL pulses corresponding to forward-to-reverse transitions, but the behavior was the same for reverse-to-forward transitions. At frequencies below 5 kHz, each EL pulse decayed exponentially from its peak value and was reduced by at least a factor of  $e$  prior to the next voltage transition. Above 5 kHz, the frequency became too fast for each pulse to decay by at least a factor of  $e$ ; however, a peak still occurred followed by a partial decay of the luminescence. At 50 kHz (not shown), the limited response time of the detector resulted in a flat EL response with no peak or decay. Beyond 50 kHz, the EL response remained flat but the signal began to decrease. We fit the decay time of the EL signal at each frequency using a single exponential decay, and the results are shown in Figure 8. The decay time decreased from  $\sim 70 \mu\text{s}$  at 50 Hz to less than  $30 \mu\text{s}$  at 5 kHz. The decay time of the 10 and 25 kHz signals could not be extracted due to the limited response time of the detector.

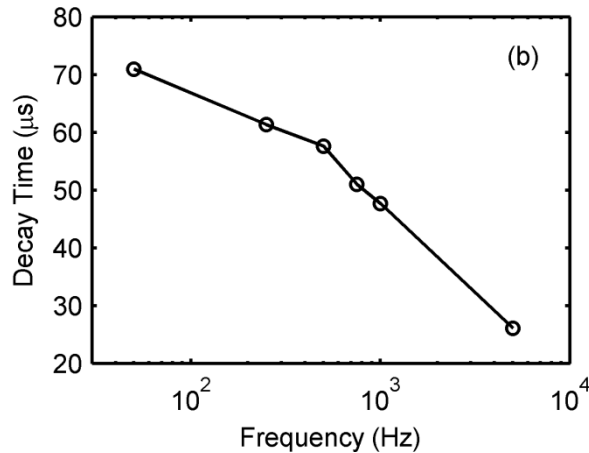


**Figure 8.** The decay time of the EL spikes decreases at high frequency. After [12].

In order to quantify the advantage of a pulsed pumping scheme over a DC pumping scheme, we measured the light output as a function of voltage for DC pumping and the light output as a function of rms voltage at 1 kHz for pulsed pumping (Figure 9(a)). We measured the output power using a separate optical power detector that required the measurements to be taken at 1 kHz due to speed limitations. For rms voltages below 30 V, the corresponding DC current that would flow through the devices was less than  $0.15 \mu\text{A}/\text{cm}^2$ , and the corresponding DC EL output was less than 20 pW. As the voltage increased sufficiently to allow for a significant DC current, the DC driven output and the pulsed driven output began to converge. In Figure 9(b), we present the output power enhancement in the pulsed pumping scheme as compared to the DC pumping scheme, and we note a maximum enhancement factor of 18 at 30 V. At higher voltages, this enhancement decreases due to the increasing amount of DC current flowing through the device. However, high DC driving voltages and current densities can hurt the long-term performance of Si-nc LEDs. Therefore, a pulsed pumping scheme offers an opportunity to increase the reliability of such devices by improving performance sufficiently to allow for operation at lower voltages.

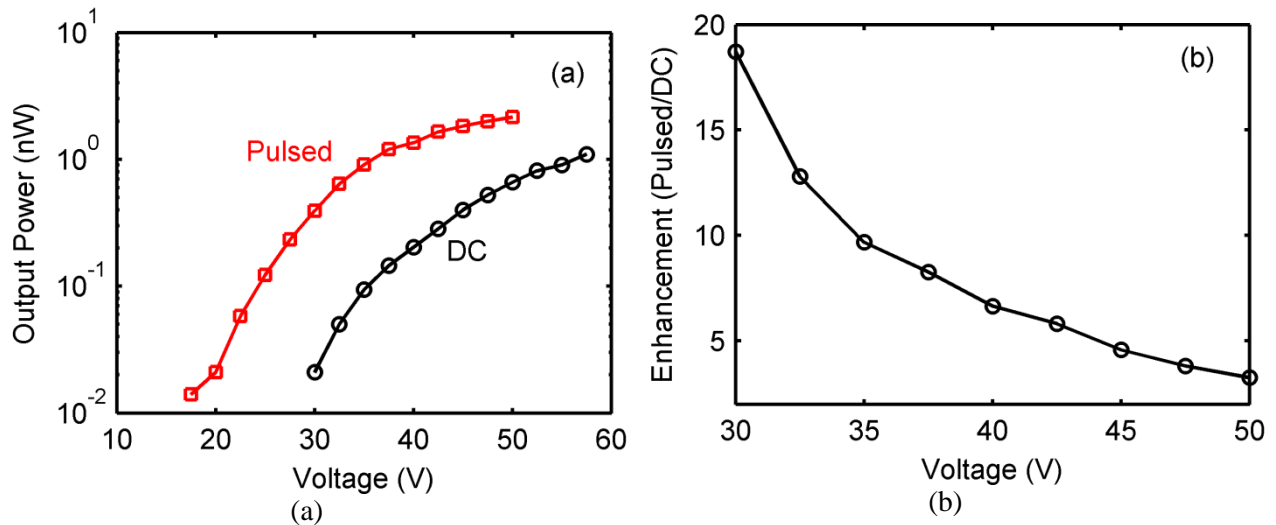


**Figure 9.** (a) Output power of Si-nc LED under pulsed and DC excitation. (b) The enhancement in the output power using the pulsed excitation mechanism decreases as a function of voltage; nonetheless, the pulsed injection mechanism outperforms DC excitation by an order of magnitude at low voltages where the device is most stable. After [12].

#### 4.1.3 Modeling Si nanocrystal based devices

While the structural and optical properties of low dimensional silicon based materials have been widely investigated and reported in the literature, their incorporation in active photonic devices has been limited. The design of active devices based on these materials will rely on the interaction of the quantum mechanics based material properties with device dictated electromagnetic fields. We developed a modeling tool to aid in this transition based on a coupled quantum and electromagnetic modeling technique, where atoms in active systems are treated quantum mechanically while the electromagnetic wave is treated classically. In this way, light interaction with an active medium can be fully understood using a classical harmonic

oscillator model and the rate equations of electron population density. To study the temporal dynamics of these systems we employ the finite-difference time domain (FDTD) method in conjunction with a set of auxiliary differential equations (ADE) which allow us to represent the material's quantum behavior by a four-level rate equation model [13]. A flow chart of this method is shown in Fig. 10.

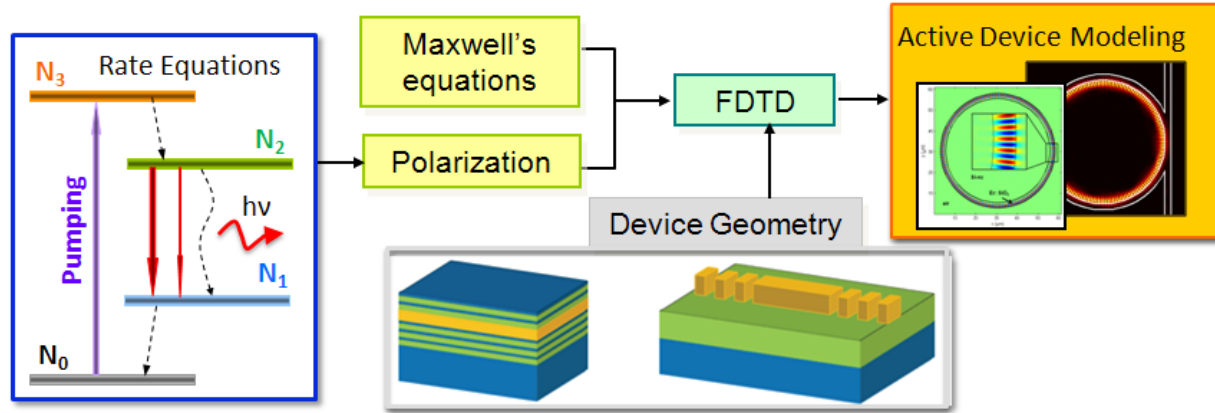


**Figure 10.** Schematic of the ADE-FDTD modeling technique. The active material's gain and absorption is dictated by a rate equation model and coupled with Maxwell's equations within the FDTD framework to provide active device level modeling.

This modeling tool allows us to study active device behavior such as amplification, enhanced spontaneous emission and lasing. In general it can be applied to any light emitting material for which an accurate rate equation model is known. As in a conventional FDTD simulation, each mesh point in the computational space has an associated dielectric constant and loss coefficient (treated as conductivity), which are constant in time. Each mesh point also has an associated electric and magnetic field component which are adjusted at each time step. In the ADE-FDTD scheme, each mesh point also has a set of energy level populations,  $N_{1-4}$ , and a macroscopic polarization term,  $\mathbf{P}$ . At each time step, we update not only the electromagnetic fields, but also the energy level populations and the polarization. The electromagnetic fields at a given mesh point are dictated by their usual interaction with neighboring fields and with a source term,  $\mathbf{J}$ , and the polarization,  $\mathbf{P}$ . The polarization is determined by the electric field and the population inversion at a given mesh point. The energy level populations are determined by the parameters of the gain material's rate equation model, the external pumping rate,  $W_p$ , as well as the polarization and electric field. This process is depicted in Fig. 11.

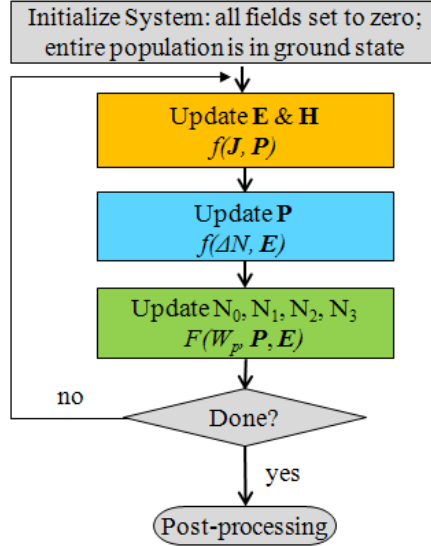


**Figure 11.** Flowchart for the ADE-FDTD simulations. At each timestep, this process is followed at each mesh point.

At the beginning of a simulation, the entire energy level population, at each mesh point in the active material, is in the ground state. The electromagnetic waves are governed by Maxwell's equations:

$$\begin{aligned}\nabla \times \mathbf{E}(t) &= -\mu_0 \frac{\partial \mathbf{H}(t)}{\partial t} \\ \nabla \times \mathbf{H}(t) &= \varepsilon_0 \varepsilon_r \frac{\partial \mathbf{E}(t)}{\partial t} + \frac{\partial \mathbf{P}(t)}{\partial t} + \mathbf{J}(t),\end{aligned}\quad (3)$$

where  $\mathbf{E}$  is the electric field,  $\mathbf{H}$  is the magnetic field,  $\mathbf{P}$  is the induced macroscopic polarization and  $\mathbf{J}$  is a source term. Each of these terms are defined for each grid point and are updated at each time step. Each grid point also has the following associated material properties:  $\mu_0$ , the magnetic susceptibility;  $\varepsilon_0$ , the electric susceptibility; and  $\varepsilon_r$ , the relative dielectric constant. Note that the polarization in this expression represents the interaction with the gain material and is not the due to the electronic polarization in the dielectric medium, thus the relative dielectric constant remains in the equation. The polarization is defined as

$$\frac{d^2 \mathbf{P}(t)}{dt^2} + \Delta \omega_s \frac{d\mathbf{P}(t)}{dt} + \omega_s^2 \mathbf{P}(t) = \kappa \Delta N(t) \mathbf{E}(t), \quad (4)$$

where  $\omega_s$  is the center emission frequency,  $\Delta \omega_s$  is the emission linewidth, and  $\Delta N$  is the population inversion. The dependence of polarization on both the electric field and the population inversion thus provides the link between the material gain or absorption and the field strength. In order for simulated emission to occur, an electromagnetic field ( $\mathbf{E}$ ) must be present in a material with a population inversion  $\Delta N < 0$ . This situation will induce a polarization which subsequently manifests as an amplification term affecting the electromagnetic fields in Eqn. 3. If a field is present in a material with a positive population inversion, stimulated absorption will result. The strength of this interaction is dictated by  $\kappa$ , which is a defined as

$$\kappa = c\epsilon_0 n \sigma_s \Delta\omega_s, \quad (5)$$

where  $c$  is the speed of light,  $n$  is the refractive index, and  $\sigma_s$  is the absorption or emission cross section, depending on the sign of the population inversion. Thus, the absorption or gain introduced by interaction between an electromagnetic field and a material with a given population inversion is scaled by the absorption or emission cross section.

The remaining terms account for the rate equation dynamics of the Si-nc material. Optical gain in Si-nc films has been modeled using a four-level rate equation system, as shown in Fig. 12 [14].

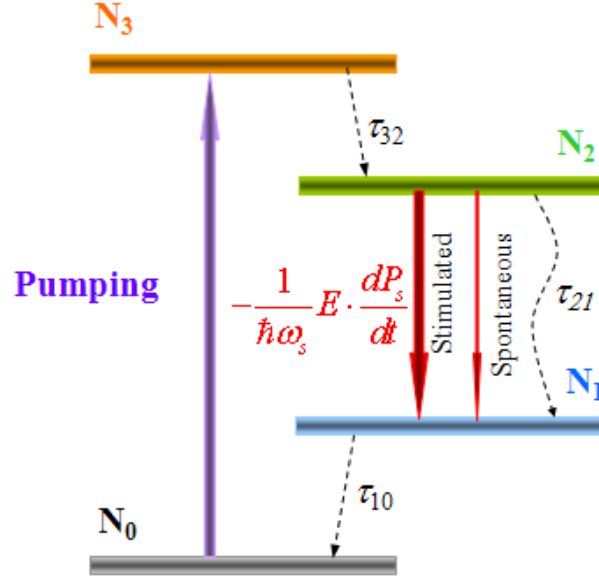


**Figure 12.** The Si-nc emission and gain behavior is dictated by a four-level rate equation model where the radiative transition occurs between  $N_2$  and  $N_1$ .

The corresponding rate equations are defined as:

$$\begin{aligned} \frac{dN_3(t)}{dt} &= -\frac{N_3(t)}{\tau_{32}} + W_p N_0 \\ \frac{dN_2(t)}{dt} &= \frac{N_3(t)}{\tau_{32}} - \frac{N_2(t)}{\tau_{21}} + \frac{1}{\hbar\omega_s} \mathbf{E}(t) \cdot \frac{d\mathbf{P}(t)}{dt} \\ \frac{dN_1(t)}{dt} &= \frac{N_2(t)}{\tau_{21}} - \frac{N_1(t)}{\tau_{10}} - \frac{1}{\hbar\omega_s} \mathbf{E}(t) \cdot \frac{d\mathbf{P}(t)}{dt} \\ \frac{dN_0(t)}{dt} &= \frac{N_1(t)}{\tau_{10}} - W_p N_0 \end{aligned} \quad (3)$$

where the radiative transition between levels  $N_2$  and  $N_1$  is centered at 800 nm with a linewidth of  $\sim 100$  nm. The pumping rate which factors into the rate equations is defined as  $W_p = \sigma_{abs} I_p / \hbar\omega$  where  $I_p$  is the pump intensity and  $\sigma_{abs}$  is the absorption cross section at the pump frequency  $\omega_p$ . Note that while we define the pumping rate here as an optical pumping rate, we could also correlate  $W_p$  to an electrical pumping rate in terms of current density and electrical excitation

cross section. Our simulations of Si-nc devices were performed in terms of a general pumping rate  $W_p$  and can therefore be applied to either optically or electrically excited devices.

The first device we consider is a one dimensional microcavity, designed for enhanced spontaneous emission. Spontaneous emission is introduced as randomly oriented dipoles in the active material whose strength is proportional to the pumping rate dependent population inversion. The cavity consists of a Distributed Bragg Reflector (DBR) above and below the Si-nc region. The DBR is designed to open a bandgap around the Si-nc emission peak of 800 nm. It consists of alternate low index  $\text{SiO}_2$  ( $n=1.5$ ) and high index poly-Si ( $n=3.5$ ) with thicknesses of 125 nm and 55 nm. The thickness of the Si-nc region determines the position of the resonant mode and is chosen as 220 nm, positioning the mode near 800 nm. We first simulated the reflectance of the proposed device in a passive FDTD simulation by introducing a Gaussian pulse and recording the transmission spectrum, as shown in Fig. 13(a). The broad bandgap and resonant mode are evident. We then introduced spontaneous emission within our ADE-FDTD model and detected the luminescence above the top DBR. The luminescence for cavities with varying periods of DBR above and below are compared to the luminescence of a layer of Si-ncs directly on the substrate. The detected luminescence from DBR microcavities is shown in Fig. 13(b). The cavity emission exhibits a narrower spectrum, related to the Q of the microcavity and a peak luminescence as much as 15 times stronger than the reference Si-nc emission.

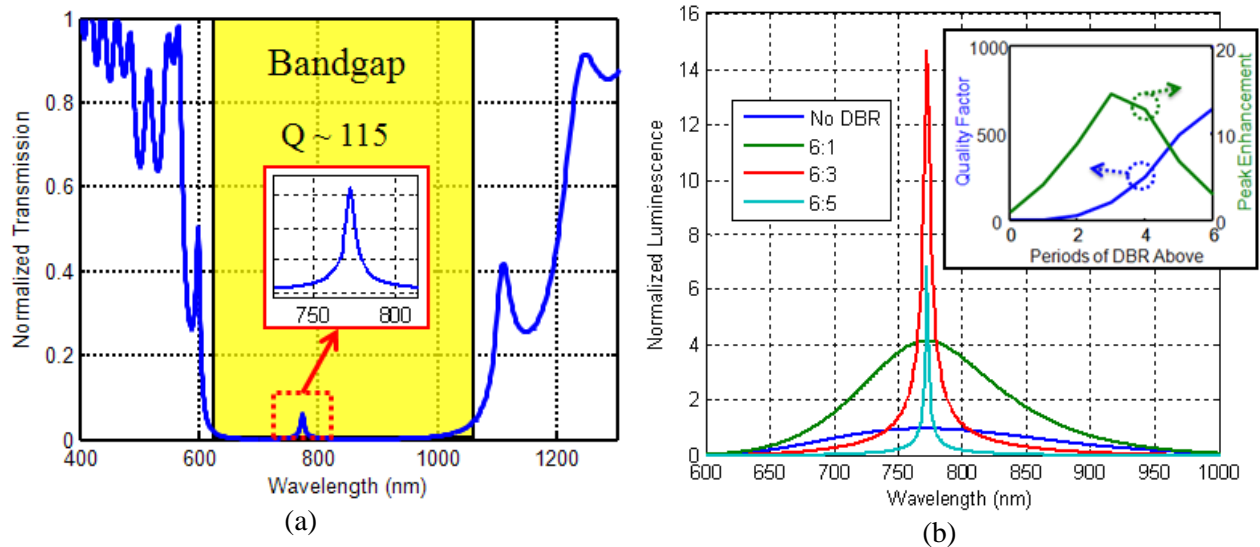


**Figure 13.** (a) Transmission spectrum for a plane wave launched from free space and propagating through a silicon nano-crystal microcavity. A bandgap with a cavity mode is observed. (b) Enhanced spontaneous emission with microcavities consisting of 1D DBRs with different number of periods.

We then investigated Si-nc waveguide based devices for in-plane amplification and emission. Each of these devices relies on the index contrast between the Si-nc film and a  $\text{SiO}_2$  substrate (or thick buffer layer on Si). The first Si-nc waveguide device we considered was an amplifier. In this case, we introduced an external source to the left of a 10  $\mu\text{m}$  long, 200 nm thick Si-nc on  $\text{SiO}_2$  waveguide and detect the transmitted signal in air to the right of the waveguide. We considered both TE (electric field in the plane of the waveguide) and TM (electric field normal to the plane of the waveguide) polarized sources. A schematic of this

configuration is shown in the inset of Fig. 14. In this analysis, we treat the Si-nc waveguide as a slab and use the bulk Si-nc index. In Fig. 14, we present the spectral response of the signal measured at the detector for different pumping rates and polarizations.

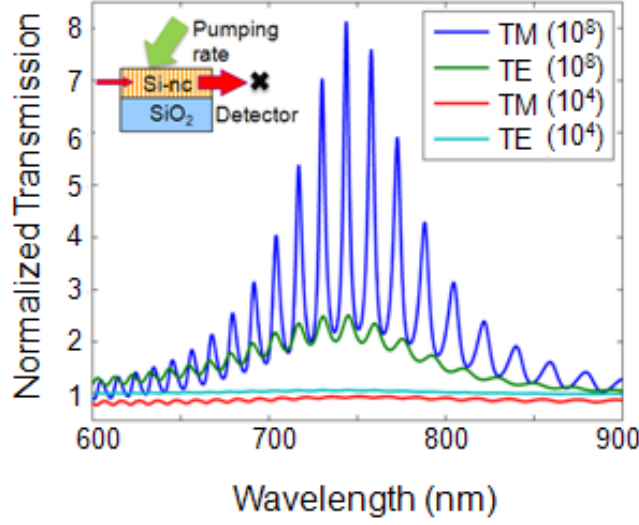


**Figure 14.** Amplification spectra through a pumped Si-nc waveguide for TE and TM polarized sources. The inset shows a schematic of the simulated device configuration. The detected signal in each case is normalized to the detected signal without pumping or material loss to eliminate the effect due to reflection at the waveguide interfaces. The pumping rate,  $W_p$ , is indicated in parenthesis. After [15].

The oscillations in the signal are due to Fabry-Perot effects at the Si-nc/air interfaces. The signal registered at the detector was normalized in each case to the detected signal for an identical source passing through the same Si-nc waveguide with the material losses removed and the pumping rate set to zero. This normalization corrects for the amount of signal reflected at the Si-nc/air interfaces and allows us to study the amplification within the waveguide region. We note that under high pumping rates,  $W_p \sim 10^8 \text{ s}^{-1}$ , corresponding to nearly 100% population inversion, both the TE and TM polarized sources experience significant amplification. The TM polarized source is nearly 8 times stronger than the reference signal while the TE source is only 2.5 times stronger. To understand this discrepancy, we considered the amplitude of the steady state field for each combination of polarization and pumping rate, as shown in Fig. 15. We observe that the TM mode experienced a higher degree of confinement within the Si-nc region and attribute the increased amplification to this improved modal overlap with the gain medium. The steady state field also shows the enhancement of the fields as they propagate from left to right along the waveguide. The nodes in the field indicate a weak resonance due to the reflections at the air/Si-nc interface.

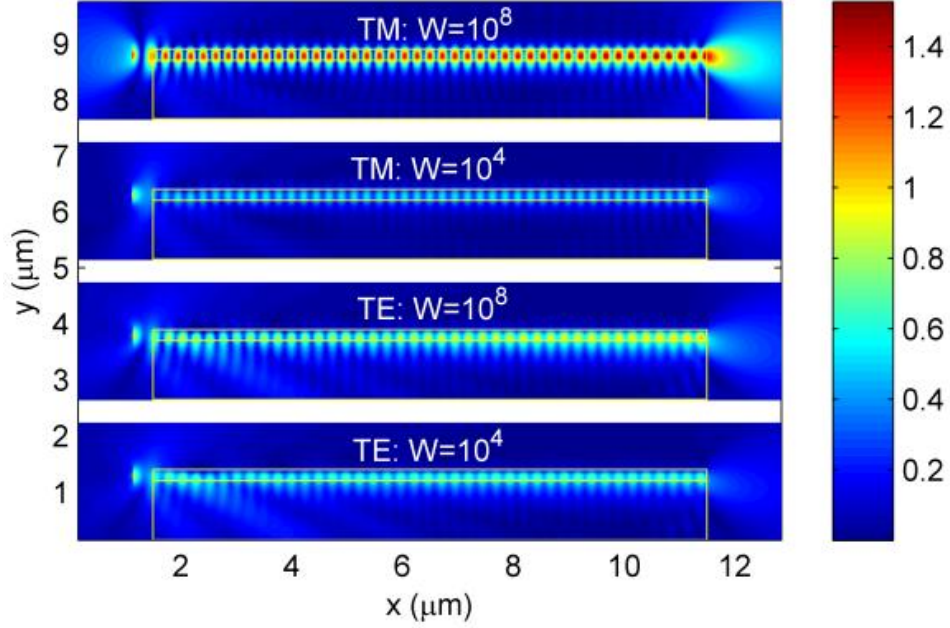


**Figure 15.** The amplitude of the steady state field at the peak wavelength of 750 nm for TE and TM polarized sources under different pumping rates. The nodes in the field along the length of the interface are due to Fabry-Perot resonances at the Si-nc/air interfaces. After [15].

Si-nc waveguides can be used not only for amplification but also as a light source in their own right. We therefore investigated enhanced spontaneous emission in these Si-nc waveguides. As noted above, the Si-nc/air interface already provided a weak Fabry-Perot cavity in the Si-nc waveguide. In order to improve the quality factor of the Fabry-Perot cavity, we increased the reflectance at the edges of the Si-nc waveguide by introducing DBRs, similar to those investigated in vertically emitting DBR microcavity. In this case the DBRs needed to be normal to the waveguide and thus we achieved an index contrast by “etching” holes through the Si-nc layer and 200 nm into the SiO<sub>2</sub> substrate. The DBRs then consisted of alternating layers of Si-nc and air. The width of the Si-nc and air regions in the DBR was set to a quarter of a wavelength in the respective materials. The center Si-nc waveguide region was set to be 5 μm. We considered cavities with three periods of DBR on either side, requiring three etched regions, as shown in the inset of Fig. 16. We introduced spontaneous emission in the center Si-nc region and detected the luminescence signal in the air to the right of the cavity. The collected luminescence for TE and TM polarized spontaneous emission in the DBR cavities was normalized to the signal collected for the same 5 μm Si-nc waveguide without DBRs and is shown in Fig. 16.

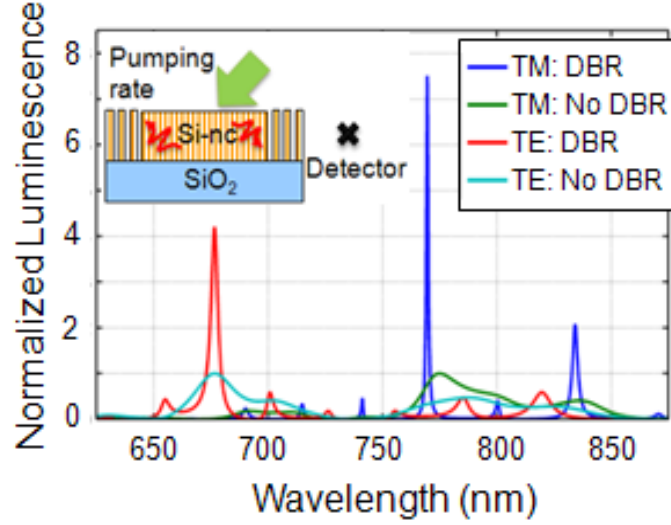


**Figure 16.** The enhanced spontaneous emission collected for TE and TM modes with and without 3 periods of DBRs. The microcavities exhibited a PL enhancement factor of 4 in the TE case and 7 in the TM case. After [15].

The peak luminescence in the cavity was enhanced by a factor of 4 for the TE polarization and more than 7 for the TM polarization. We also note that the linewidth of the TM polarized mode is significantly narrower than that of the TE polarized mode. Both the decreased enhancement and larger linewidth of the TE mode indicate a lower quality factor, a result of reduced reflection at the DBRs. The reduced reflection in the TE case is due to its larger mode extension into the SiO<sub>2</sub>, which allows energy to leak out of the cavity through the substrate. The relative strengths of the TE and TM modes are evident in the amplitude of their respective steady state fields, shown in Fig. 17. It is also clear that the confinement is significantly enhanced by the presence of the DBRs. This structure provides the ability to enhance the spontaneous emission from a Si-nc film and provide a relatively narrow linewidth source in the plane of the sample.

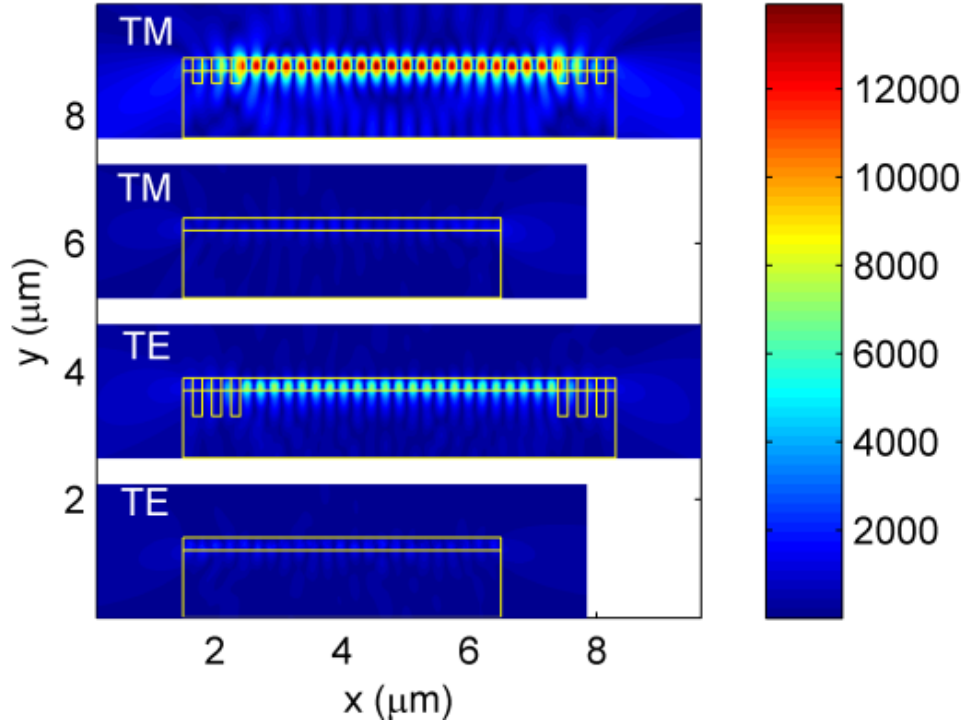


**Figure 17.** The amplitude of the steady state field at the peak wavelength for the indicated polarization is shown with and without DBRs. The field is clearly enhanced in the cavities with DBRs. After [15].

#### 4.1.4 Integrated Si nanocrystal based light emitting devices

In this section, we present our experimental work fabricating devices using Si-ncs as the active material. The first device we considered was a 1D DBR microcavity based on the simulations presented in the previous section. The entire film was deposited on a Si substrate via PECVD. The poly-Si and SiO<sub>2</sub> layers in the DBR are deposited using the same PECVD recipe as the a-Si and SiO<sub>2</sub> layers in the Si-nc superlattice. A subsequent 1 hour furnace anneal at 1100° C precipitates the nanocrystal formations in the Si-nc film and crystalline formations in the a-Si, transforming it to poly-Si. A cross sectional scanning electron microscope (SEM) of a fabricated cavity is shown in Fig. 18(a). Note that the sample depicted in Fig. 18(a) is a calibration sample and the thicknesses and number of layers in this calibration sample are different from the optimized sample discussed in the remainder of this section. Nonetheless, the SEM shows the general structure and reveals the increasing roughness of layers further from the substrate. This increase in roughness with total deposition thickness limits our ability to increase the cavity-Q simply by adding more periods to the DBRs, as predicted by our simulations.

After calibrating the deposition rates, we fabricated devices with 6 periods of DBR below the Si-nc layer and 1 to 4 periods of DBR above. We performed active characterization by exciting the cavity from above with a 532 nm laser and collecting the PL from above with a spectrometer. The normalized PL spectra and the enhancement relative to the reference Si-nc film are shown in Fig. 18(b). The Q values and the enhancement factor both increase with the number of DBR periods above the Si-nc layer. We observed a peak enhancement factor of 15

compared to the peak of the Si-nc film without a cavity for the device with 6 periods of DBR below and 4 above.

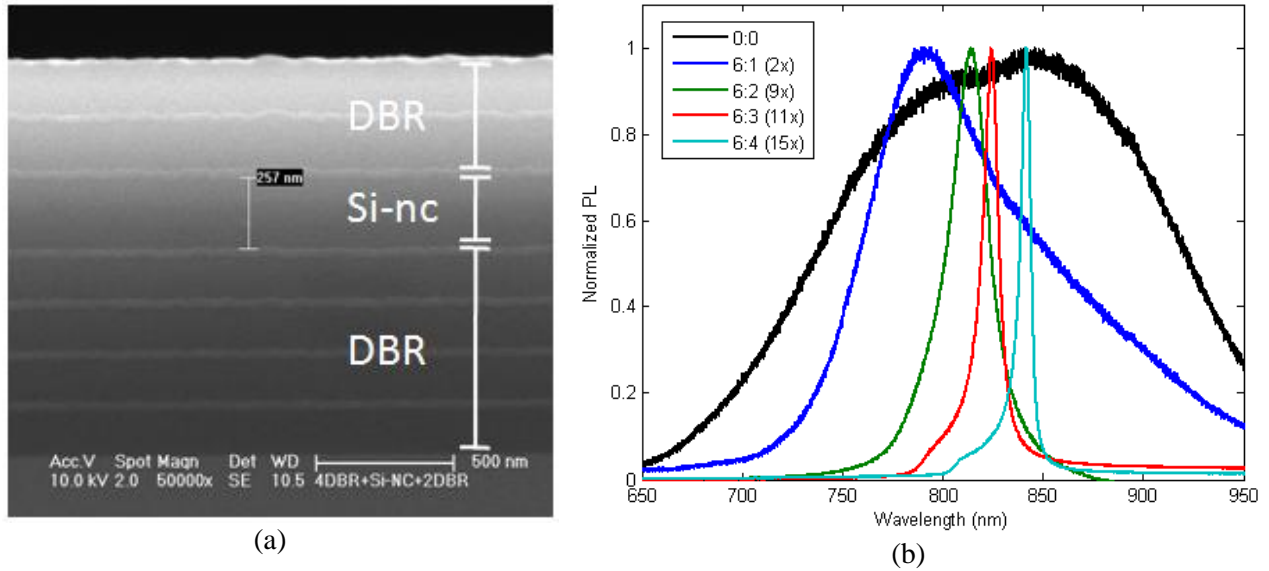


**Figure 18.** (a) Cross sectional SEM of a fabricated Si-nc DBR microcavity. The Si layers are light and the SiO<sub>2</sub> and Si-nc layers are dark. (b) The normalized PL spectra of the reference Si-nc layer and DBR cavities. The enhancement factor is noted in parenthesis in the legend.

This behavior was in excellent agreement with our simulated predictions, presented in the previous section. As we also noted in the previous section, these devices should perform similarly under optical or electrical excitation. To confirm this, we developed a fabrication process to allow for electrical excitation of a Si-nc DBR microcavity. Fabrication of the electrically pumped DBR microcavity proceeded as follows: First, a 4-period DBR consisting of SiO<sub>2</sub> and a-Si layers with thicknesses of 200 nm and 45 nm, respectively, was deposited by PECVD. Next, a 115 nm a-Si layer was deposited and the sample was annealed at 1100 °C in an N<sub>2</sub> environment for 2 hours to form polycrystalline Si (poly-Si). The poly-Si layer was doped with phosphorous by diffusion at 900 °C using phosphorous oxychloride (POCl<sub>3</sub>) as a diffusion source. After diffusion of the lower contact layer, a Si-nc layer with a total thickness of 50 nm was deposited followed by another 115 nm a-Si layer to serve as the second contact layer. A second high temperature anneal at 1100 °C for 2 hours formed nanocrystals in the active layer and poly-Si in the contact layer. A second diffusion step, identical to the first, served to dope the second contact layer with phosphorous. After this diffusion, a 2-period DBR with SiO<sub>2</sub> and a-Si layer thicknesses identical to the initial DBR was deposited to complete the cavity structure. A reference sample was fabricated without DBR layers. Fluorine based dry etching processes were used to define the active area of the device (a circle with a diameter of 600 μm) and to etch vias for access to the doped layers inside the DBR cavity. Finally, Ti/Au contacts were established using a lift-off process. A schematic of the final device is shown in Fig. 19(a).

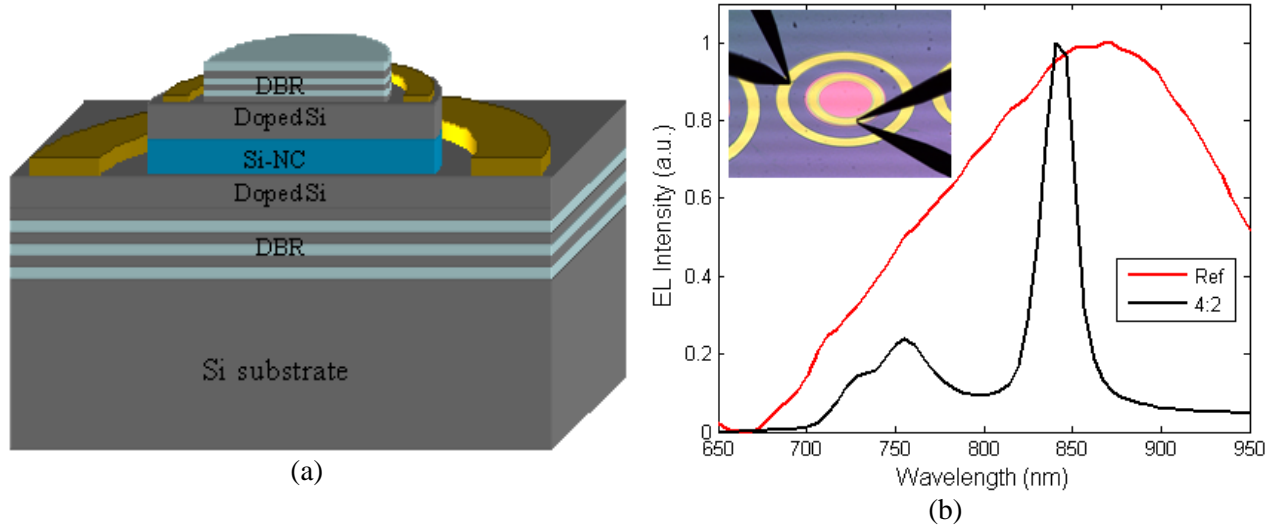


**Figure 19.** (a) Schematic of the electrically pumped Si-nc DBR microcavity. (b) The normalized EL spectra of the reference device and the DBR cavity. The inset shows the tested structure with probe tips contacting the gold rings.

EL was collected from these devices by contacting the Au rings and applying a DC voltage. The EL spectrum collected from the microcavity was normalized to the EL collected from the reference device and is shown in Fig. 19(b). The peak of the EL in the DBR device was a factor of 25 stronger than the peak of the reference device. The DBR device also showed similar line narrowing to the optically pumped devices. We then compared the external quantum efficiency of the electrically pumped DBR device to the reference device. The external quantum efficiency was defined as  $\eta_{ext} = P_0 \times q / (I \times h\nu)$  where  $P_0$  is the output power (integrated over all wavelengths),  $q$  is the charge of an electron,  $I$  is the current,  $h$  is Planck's constant, and  $\nu$  is the frequency. The external quantum efficiency as a function of current density is shown in Fig. 20. The DBR device resulted in a factor of 2 improvement in the external quantum efficiency.

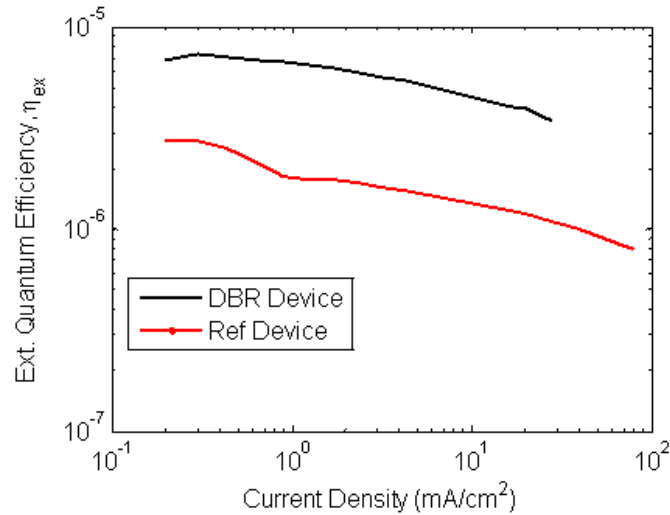


**Figure 20.** External quantum efficiency for the electrically pumped DBR cavity and the reference device.

Although these DBR microcavities performed well, their out-of-plane emission limits their usefulness in an integrated photonics sense. We therefore investigated a series of in-plane Si-nc microdisk type devices. Microdisks support high Q modes called whispering gallery modes (WGMs). The basic Si-nc microdisk structure was fabricated as follows: We began by depositing a Si-nc film on a Si substrate, following the superlattice technique described above. We then patterned the disks in AZ5214-E resist using conventional photolithography. We applied an inductively coupled plasma (ICP) etch process based on a  $C_4F_8$ ,  $SF_6$  and Ar environment to transfer the disk pattern into the Si-nc film. A second ICP etch process in a  $SF_6$  environment selectively etched the underlying Si substrate, thereby isolating the Si-nc microdisk from the substrate. An SEM of a fabricated Si-nc microdisk is shown in Fig. 21.

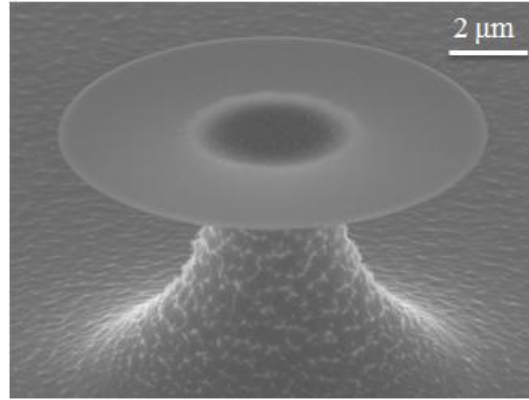


**Figure 21.** SEM of a fabricated Si-nc microdisk suspended on a Si pedestal.

In order to characterize the modal structure of the Si-nc microdisks, PL was collected in the plane of the disk using free space optics [16]. PL was generated by illuminating the disk from above with a focused 532 nm laser. A schematic of this collection setup is shown in Fig. 22 along with a photograph of the experimental setup. The first collection lens, focused on the edge of the disk, collimated the Si-nc PL signal. A second lens focused the Si-nc PL onto the entrance slit of the spectrometer. An optional polarizer was incorporated in the collimated region between the lenses enabling us to take polarization dependent measurements. Experimentally, we constructed a breadboard on a “Global” XYZ stage which supported both the sample and the laser (and associated laser optics: a beam expander, lens and mirror). This global positioning allowed us to align the excited sample with respect to the collection optics. This method was necessary because the collection optics, once aligned to the spectrometer, could not be moved. In this way, we performed the final alignment by moving the sample and laser stage until the PL signal reached a maximum. A separate “Local” XYZ stage allowed us to move the sample under the laser once alignment was achieved so that we could probe different devices. A charge coupled device (CCD) camera with a 20x objective imaged the microdisk sample and laser spot from above.

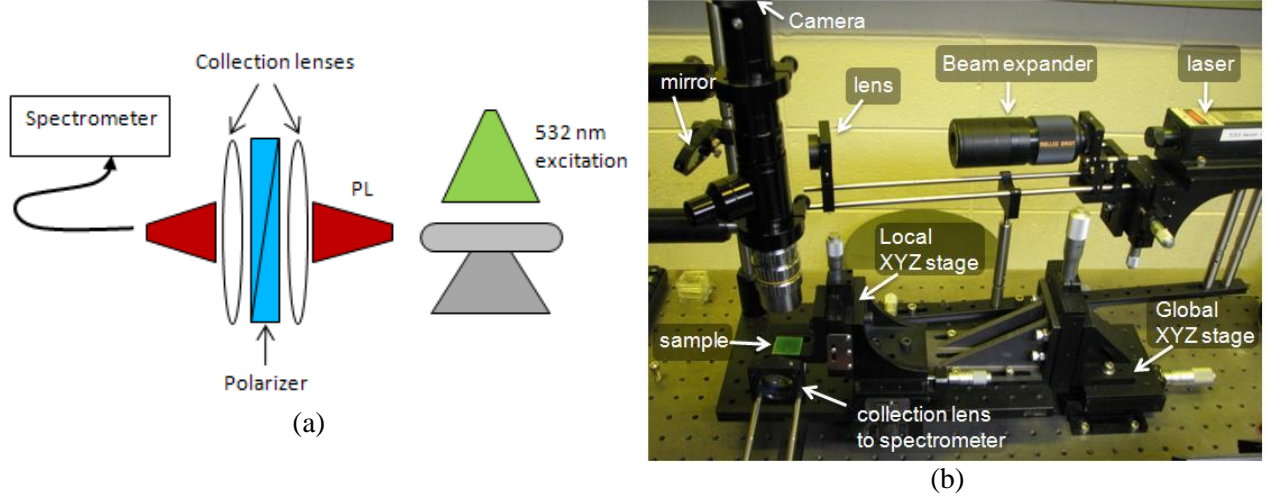


**Figure 22.** (a) Si-nc microdisk WGMs were characterized by collecting PL from the edge of the disks with two collection lenses. The first lens was aligned to the edge of the disk and the second lens was aligned to the entrance slit of the spectrometer. An optional polarizer was incorporated to filter the PL signal. (b) Photograph of the experimental characterization setup.

The collected PL spectrum, shown in Fig. 23, revealed the existence of WGMs with varying azimuthal modes across the Si-nc emission region. We also observed a background bias due to PL from Si-ncs which did not contribute to WGMs. The WGMs exhibited quality factors of  $\sim 2 \times 10^3$ , limited by the spectral resolution of our spectrometer. A close-up of one of these modes is shown in Fig. 23(b).

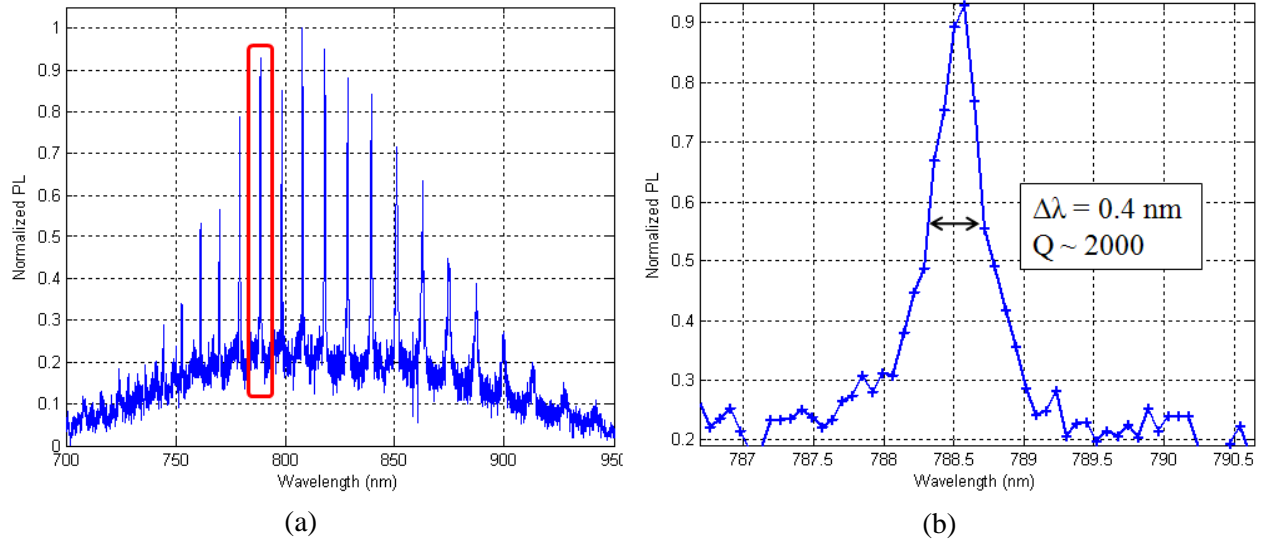


**Figure 23.** (a) PL spectrum collected using the far-field technique from a 100 nm thick, 15  $\mu\text{m}$  diameter Si-nc microdisk. The PL spectrum reveals WGMs with varying azimuthal order. (b) Close up of the mode indicated by the red box in (a) showing a  $Q \sim 2 \times 10^3$ , limited by the resolution of our spectrometer..

One of the drawbacks of the Si-nc light emitting devices presented thus far is their visible wavelength emission. In order to interface Si-nc based devices with other photonic devices, particularly those which rely on Si waveguides, emission at  $\sim 1500$  nm is highly desirable. For

this reason, researchers have investigated incorporation of erbium ions, capable of light emission at 1500 nm, in Si-nc films [17]. Unfortunately, Si-nc films have also been found to exhibit a high free carrier absorption cross section, thereby introducing an additional loss mechanism at high pumping powers which could prohibit lasing [18]. In an effort to convert the Si-nc emission to 1500 nm without subjecting the erbium based telecommunication wavelength emission, we designed a concentric microdisk structure [19].

The concentric microdisk structure consists of an inner disk of Si-nc surrounded by an outer ring of Er:SiO<sub>2</sub>, as shown schematically in Fig. 24(a). The first order radial whispering gallery modes excited by the erbium ions at 1500 nm will exist in the outer ring and therefore avoid interaction with the Si-ncs and any associated losses. This type of Er:SiO<sub>2</sub> based mode is very similar to that which lives in Er:SiO<sub>2</sub> microtoroid and microdisk lasers [20]. We therefore expect that the outer ring in our concentric microdisk design should support an erbium based laser operating at ~1500 nm if sufficient optical pumping is achieved. Pumping thresholds as low as a few  $\mu$ W have been achieved for resonant ~1480 nm pumping of Er:SiO<sub>2</sub> toroids [20]. In the concentric microdisk design, we seek to replace this external optical pump with EL from the Si-nc inner disk. Based on FDTD simulations, we expect that luminescence from the inner Si-nc disk will excite higher order radial WGMs extending into the Er:SiO<sub>2</sub> region [19]. The Si-nc emission peaks at ~800 nm, which corresponds to an erbium absorption line. Thus electrical pumping of the Si-nc inner disk will generate ~800 nm modes which will act as an optical pump to create population inversion and ~1500 nm lasing in the outer Er:SiO<sub>2</sub>.

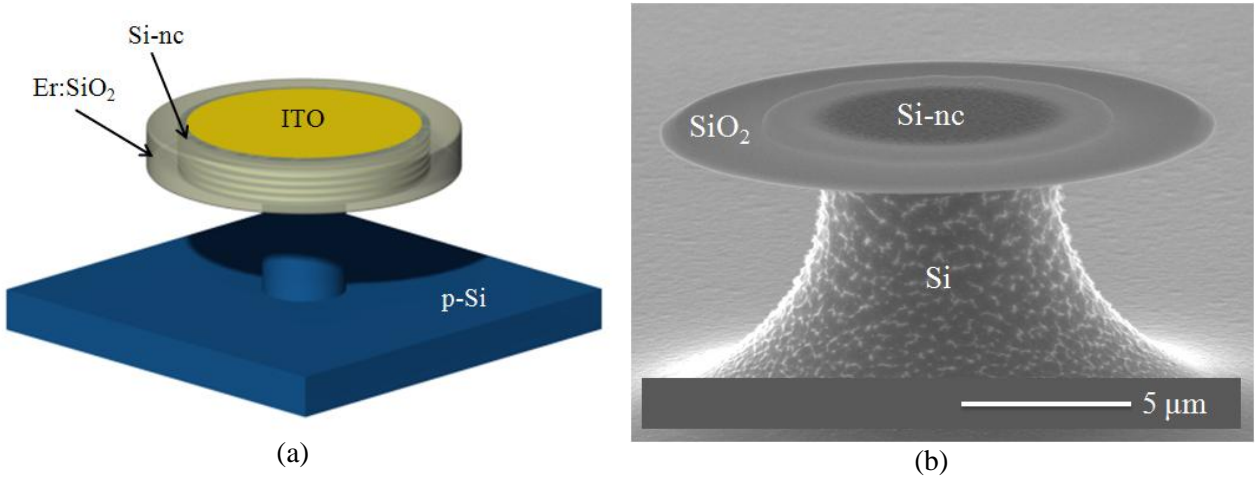


**Figure 24.** (a) Schematic of the proposed concentric microdisk structure. The transparent ITO contact on the inner Si-nc disk allows for electrical pumping of the Si-ncs. (b) SEM of a concentric microdisk consisting of an inner Si-nc disk and an outer SiO<sub>2</sub> ring on a Si pedestal. After [21].

In order to confirm that luminescence from the inner Si-nc disk will in fact excite resonant modes extending into an outer ring, we fabricated a concentric microdisk test structure. Our fabrication process began the same as the original Si-nc microdisk. We deposited the Si-nc layer on a Si substrate, patterned circles in Photoresist, and transferred the pattern into the Si-ncs using an ICP etching process. At this point, before conducting the under etch, we blanket deposited an SiO<sub>2</sub> layer in the PECVD and patterned the outer disk in Photoresist, carefully aligned on top of the original disks. We then repeated the initial ICP etch process and performed the undercut etch. The final structure is shown in Fig. 24(b).

We fabricated concentric microdisks with varying inner disk radius and outer ring width and collected PL in the Si-nc emission spectrum in the same manner as from the Si-nc microdisks considered above. We collected PL for disks with inner radii of 5.5, 6.5 and 11  $\mu\text{m}$  and  $\text{SiO}_2$  widths of 600 nm and 1200 nm. We observed clear WGM type modal structure in the PL from each disk with a 600 nm  $\text{SiO}_2$  ring; however, of the three disks with a 1200 nm  $\text{SiO}_2$  ring, only the one with the largest radius (11  $\mu\text{m}$ ) supported modes. The reason modes were not observed on the smaller radius disks with a large overhang will be discussed in light of the FDTD analysis presented below. The PL spectra collected from disks which exhibited WGM type structure are shown in Fig. 25(a). The WGMs collected exhibited quality factors as high as  $\sim 2 \times 10^3$ , limited by the resolution of our spectrometer.

In order to interpret the results presented in Fig. 25(a), we performed ADE-FDTD simulations of the fabricated device. We considered a concentric disk with a 6.5  $\mu\text{m}$  inner Si-nc radius and a 600 nm outer  $\text{SiO}_2$  width. The simulation was performed in 2D using effective indices to account for the thickness of the disks. We introduced spontaneous emission in the inner Si-nc disk and placed a detector at the edge of the outer  $\text{SiO}_2$  ring. The spectral response collected at the detector is shown in Fig. 25(b). The structure considered was too thin to support multiple axial modes; therefore, the observed modes must be described by varying azimuthal and radial mode orders. We performed additional simulations to extract the amplitude of the steady state fields at the resonances in the simulated mode spectrum. Two of these steady state fields are shown as insets in Fig. 25(b). Based on the steady state fields, we observed that the high-Q modes in this geometry are first order radial WGMs extending from the Si-nc region to the edge of the  $\text{SiO}_2$  ring and the lower-Q modes are second order radial WGMs. This result matches well with the experimental PL spectra presented in Fig. 25(a) for the same geometry: at longer wavelengths, a dominant first order radial mode was observed, and at shorter wavelengths, higher order radial modes were observed. As in the simulation, these higher order radial modes exhibited lower quality factors.

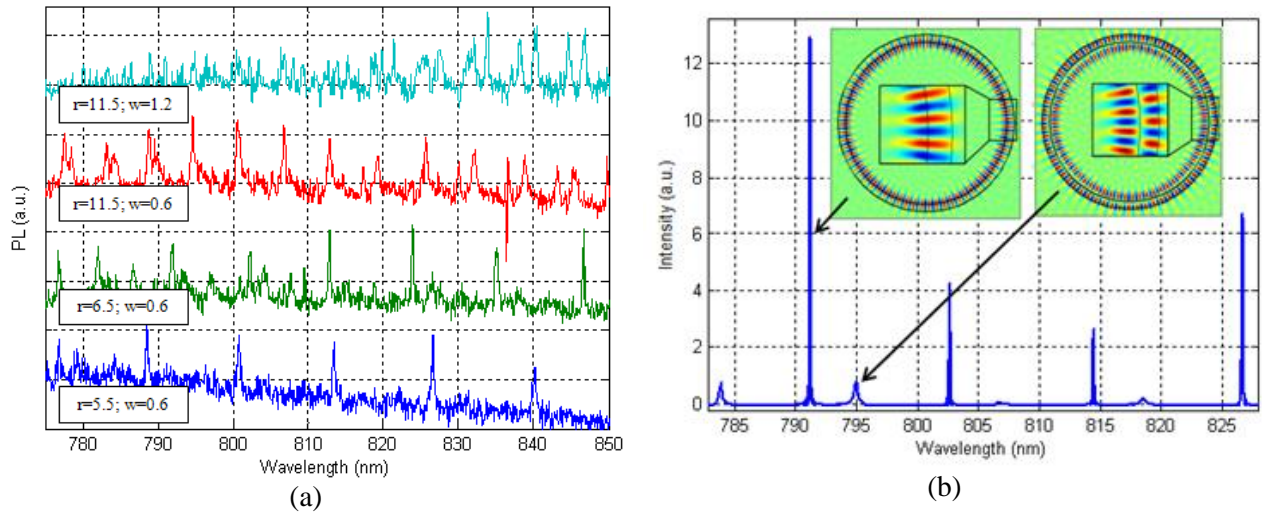


**Figure 25.** (a) Experimental PL spectra collected from concentric microdisks with inner Si-nc disk radius  $r$  and outer ring width  $w$ , both in  $\mu\text{m}$ . (b) ADE-FDTD simulation of modes excited in the Si-nc luminescence spectrum for a disk with an inner radius of 6.5  $\mu\text{m}$  and an outer ring width of 600 nm. After [21].

We also fabricated concentric microdisks with Er:SiO<sub>2</sub> outer rings and confirmed the existence of modes ~1500 nm in the erbium PL spectrum [22]. The radius of the inner Si-nc disk was 20  $\mu$ m and the outer Er:SiO<sub>2</sub> ring width was 1  $\mu$ m. We confirmed that this structure still supported pump modes in the Si-nc emission spectrum, similar to those presented above. We then used a tapered fiber collection setup to characterize the quality factor of WGMs in the erbium emission regime [16]. The PL spectrum collected from the microdisk under 532 nm excitation is shown in Fig. 26(a). The WGM structure is clearly evident, overlaid on the background erbium PL signal. The Q of these modes were limited by the resolution of our spectrometer. We were also able to study the WGMs in the erbium emission regime passively, enabling us to measure much higher quality factors than was possible using our spectrometer.

The passive measurements were conducted by coupling a tunable IR laser into one end of the tapered fiber and collecting the transmitted signal using a Ge detector at the other end. By positioning the tapered portion of the fiber in close proximity to the edge of the microdisk, the light in the fiber coupled into WGMs in the microdisk. In this way, we detected the microdisk WGMs as drops in the transmission as a function of wavelength. The collected transmission spectrum, shown in Fig. 26(b), reveals several high-Q modes within the erbium emission spectrum. These modes exhibited quality factors as high as  $2.2 \times 10^4$ , as shown in the inset of Fig. 26(b). The Q in this device was limited by surface roughness, as WGMs in Er:SiO<sub>2</sub> based disks of similar dimension have demonstrated quality factors as high as  $\sim 10^7$  [20].

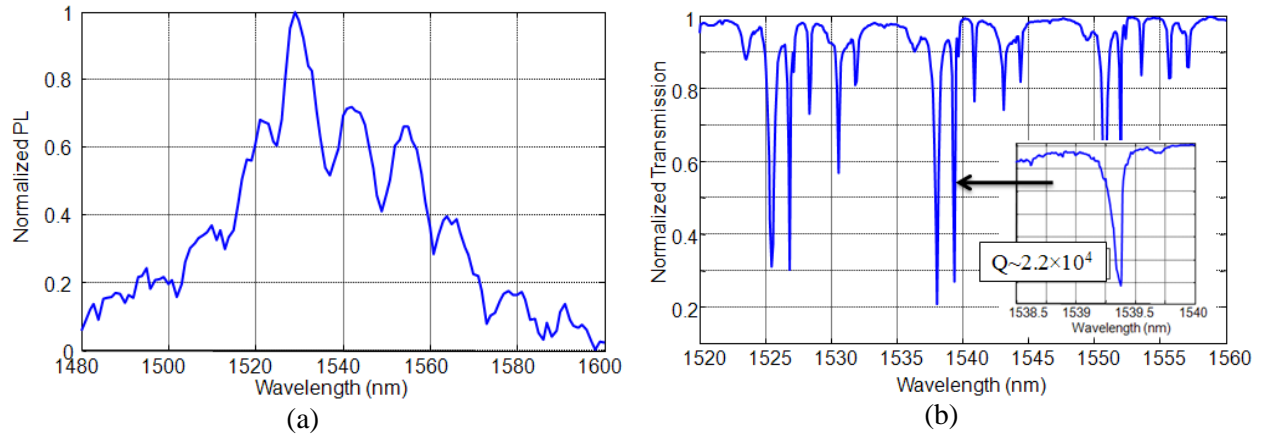


**Figure 26.** (a) Experimental PL spectra collected from concentric microdisks with inner Si-nc disk radius of 20  $\mu$ m and outer Er:SiO<sub>2</sub> ring width of 1  $\mu$ m. (b) Passive transmission spectrum measured by positioning a tapered fiber in close proximity to the concentric disk. After [22].

Unfortunately, the efficiency of the two-stage pumping in the concentric microdisk structure is limited by the spectrally narrow erbium absorption line. As a result, Si-nc luminescence which excites modes more than ~10 nm from the erbium absorption line at 800 nm will not contribute to pumping the erbium. For this reason, we investigated a microgear geometry which has the potential to select for a given azimuthal mode while suppressing undesired WGMs.

A schematic of the Si-nc microgear resonator investigated in this work is shown in Fig. 27. The microgear is defined in terms of the underlying disk thickness and radius, the number of gear teeth, the depth of the gear teeth and the duty cycle (fraction of gear to air in each period of the grating). As in the case of the microdisk presented in the previous section, the microgear is suspended on a Si pedestal in order to provide optical confinement in the vertical direction.

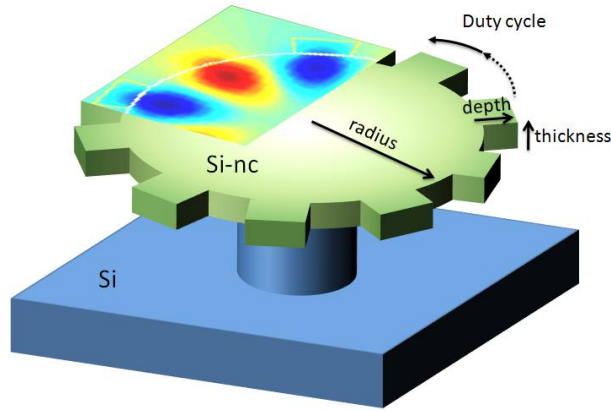


**Figure 27.** Schematic of the Si-nc microgear defined in terms of radius, thickness, gear depth and duty cycle. After [23].

Microgears provide the ability to select for a given azimuthal WGM, however, microdisks in general will support not only different azimuthal mode, but different axial and radial modes. In order to simplify our analysis, we will primarily consider microgears based on microdisks in which only the first order axial and radial modes are supported. In this regime, the remaining azimuthal modes must satisfy  $\lambda_m = \pi D_{eff} n_{eff} / m$ , where  $\lambda_m$  is the resonant wavelength of the  $m^{th}$  mode,  $\pi D_{eff}$  is the effective circumference around which the mode propagates, and  $n_{eff}$  is the effective modal index. This relationship allows us to select the resonant wavelength of a microgear by setting the number of gear teeth equal to  $2m$ .

We performed FDTD simulations to optimize the gear geometry to suppress undesired WGMs without affecting the Q of the selected WGM [23]. In accordance with our simulations, we fabricated microgears based on a  $5\ \mu\text{m}$  radius with 78 to 102 gear teeth and a  $7.5\ \mu\text{m}$  radius with 118 to 140 gear teeth. We fabricated gears with duty cycles ranging from 0.2 to 0.5 and gear depth ranging from 200 nm to 400 nm. Reference microdisks were fabricated on the same samples. The fabrication process, depicted in Fig. 28(a), was somewhat different from the microdisk fabrication process followed for the disks because of the small feature size of the gear teeth. The microgear fabrication began with a 100 nm thick Si-nc film on Si. We then exposed the gear shape in PMMA A4 resist using E-Beam lithography. After developing the resist we deposited 30 nm of Chrome via electron beam evaporation. An acetone liftoff process removed the unexposed resist, leaving a Chrome mask in the shape of our gears on the Si-nc film. We then used the same ICP etching processes used on the microdisks to transfer the pattern into the Si-nc film and undercut the Si substrate. The chrome mask was subsequently removed in a wet chrome etchant solution. An SEM of the fabricated device is shown in Fig. 28(b).

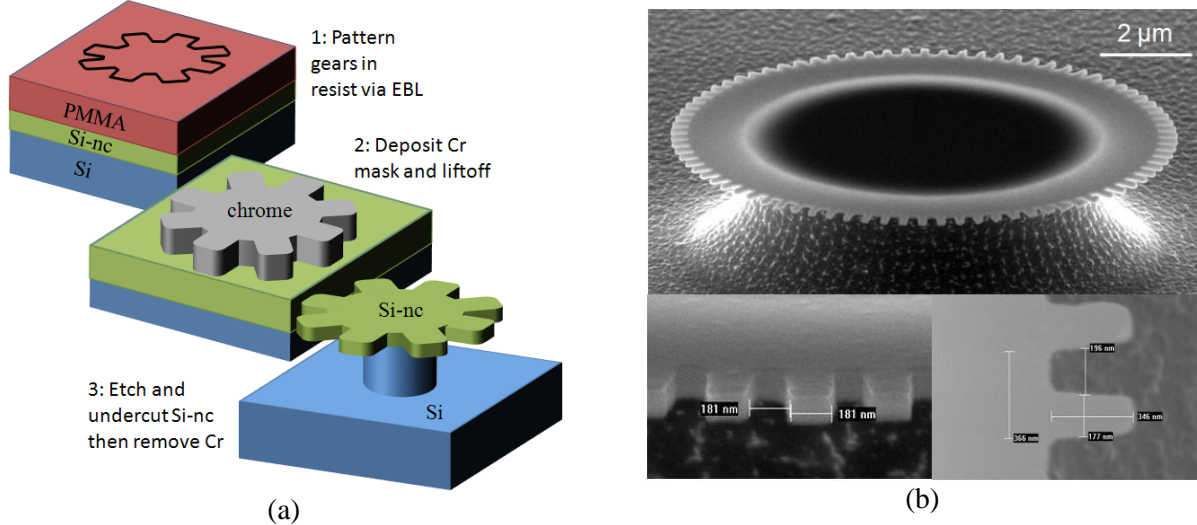


**Figure 28.** (a) Si-nc microgear fabrication process. The pattern is exposed via E-Beam lithography in PMMA resist. A 30 nm Cr etch mask is established using a liftoff process. ICP etching processes transfer the gear pattern into the Si-nc film and undercut the gear. The Cr is finally removed in a wet Cr etchant solution. (b) SEM of a fabricated Si-nc microgear on a Si pedestal. After [23].

Microgear characterization was performed by collecting PL using free space optics as in the case of the microdisks. Experimentally, we found that a 5  $\mu\text{m}$  radius microgear with 86 gear teeth supported a resonant mode near 750 nm. The PL spectra for 5  $\mu\text{m}$  radius microgears with 86 teeth, a duty cycle of 0.3 and gear depth ranging from 200 nm to 400 nm is shown in Fig. 29. We also present the PL spectrum collected from a reference microdisk. We observe that while the underlying azimuthal modes of the disk are still present in the PL spectrum for the gear with the shortest gear depth (200 nm), mode suppression increases with gear depth until only the matched mode remains. The optimal microgear geometry has a depth of 300 nm and a duty cycle of 0.3. This microgear provides a single dominant mode whose quality factor is  $\sim 300$ , comparable to that of the corresponding mode in the microdisk. The Q of both the microgear and microdisk modes is limited by bending loss.

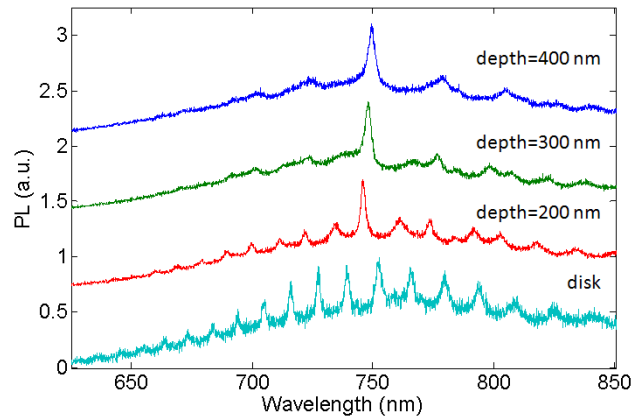


**Figure 29.** PL collected from an 86 tooth, 5  $\mu\text{m}$  radius microgear with indicated gear depth. Mode suppression increases with gear depth until a single dominant mode is evident. After [23].

We also considered the effect of varying the number of gear teeth while maintaining the optimal gear geometry (a gear depth of 300 nm and a duty cycle of 0.3). The PL spectra for microgears with 78 to 102 teeth are shown in Fig. 30, along with the reference microdisk. The matched microgear mode, circled in the figure, shifted spectrally with the number of gear teeth. This demonstrated the ability to tune the emission wavelength by selecting for various azimuthal modes. In addition, we note that even for the optimal gear geometry considered in Fig. 30, mode suppression did not cover the entire Si-nc emission region. We observe that for wavelengths  $\sim 50$  nm longer than the matched mode, the microgear supported WGMs resembling those of the underlying microdisk. At wavelengths sufficiently longer than the gear teeth, particularly with the small duty cycles considered in this work, the gear teeth were too small to interact with the modes and induce the scattering necessary for mode suppression. On the other hand, mode suppression was very effective on the short wavelength side of the matched mode. This makes sense, as modes at wavelengths much shorter than the design wavelength will continue to interact with the gear teeth.

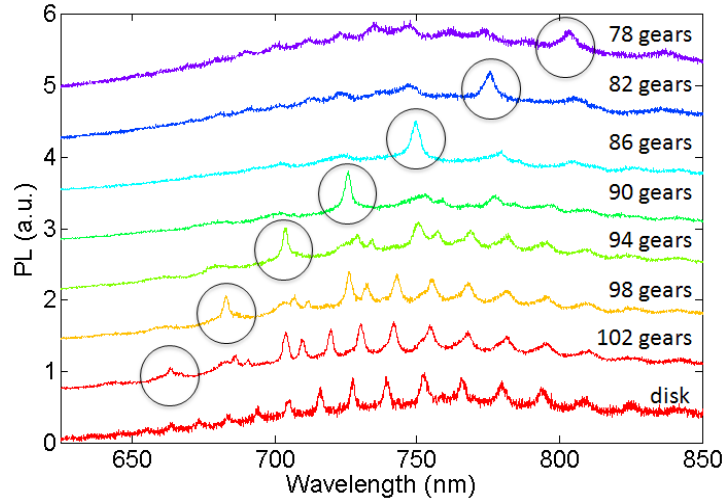


**Figure 30.** PL collected from 5  $\mu\text{m}$  radius microgears with varying number of gear teeth as indicated. The microgear clearly provides a means to select for varying azimuthal modes across the Si-nc emission spectrum. After [23].

While the 5  $\mu\text{m}$  radius microgears provided a good demonstration of the microgear effect, the  $Q$  was limited by bending loss to  $\sim 300$  which is too low for many applications. In order to reduce the bending loss we considered two approaches: increasing the radius of the gears and increasing the effective index by increasing the thickness of the Si-nc film. We first consider gears based on the same 100 nm thick Si-nc film, but with a 7.5  $\mu\text{m}$  radius. We found that the bending loss was sufficiently reduced in microdisks with this radius to support a  $Q \sim 2 \times 10^3$ , limited by the spectral resolution of our spectrometer. Due to the increased circumference, the number of gear teeth was increased to match an azimuthal mode within the Si-nc emission spectrum. We found that a microgear with 130 gear teeth, a duty cycle of 0.4 and a gear depth of 400 nm supported a mode near 800 nm. The PL spectra collected from this optimal microgear and a corresponding 7.5  $\mu\text{m}$  radius microdisk is shown in Fig. 31(a). The dominant microgear mode at  $\sim 790$  nm exhibits a quality factor of  $\sim 900$ . The microgear quality factor was reduced relative to the equivalent microdisk mode due to increased surface roughness at the gear edge. We also note the existence of two resonant modes which match the gear condition, one at 792

nm and the other at 794 nm. These modes correspond to the odd and even modes predicted in microgear simulations [24]. The even modes exhibit field extrema aligned with the gear teeth, as shown in the schematic in Fig 27, while the odd modes exhibit field extrema aligned with the space between the gear teeth. Although these modes have the same azimuthal order, their effective index is slightly different due to differences in their modal overlap with the gears, causing a shift in their resonant wavelength. This splitting may have occurred in the 5  $\mu\text{m}$  radius gears investigated above; however, due to the relatively low-Q, the two modes appeared as one. We also note that the mode suppression in the 7.5  $\mu\text{m}$  radius gear is relatively short-lived on the long wavelength side of the matched mode, while mode suppression covers nearly the entire remaining Si-nc emission spectrum on the short wavelength side.

The second approach to reducing the bending loss which limited the Q in the 100 nm thick, 5  $\mu\text{m}$  radius gears was to increase the thickness. We found that by increasing the thickness to 200 nm, 5  $\mu\text{m}$  radius microdisks exhibited spectrometer limited quality factors of  $\sim 1300$ . We fabricated a series of microgears based on 200 nm thick Si-nc films. The PL spectrum collected from a 200 nm thick microgear with 86 teeth, a duty cycle of 0.35 and a gear depth of 350 nm is shown in Fig. 31(b) along with the PL spectrum of a corresponding microdisk. The microgear exhibited a dominant mode at 783 nm, with a quality factor of  $\sim 1300$ , comparable to the Q of the corresponding microdisk. This mode was red-shifted relative to the mode in the 86 tooth, 100 nm thick microgear of the same radius because of the increased effective index. A second mode, corresponding to the odd mode, was also observed near the main resonance.

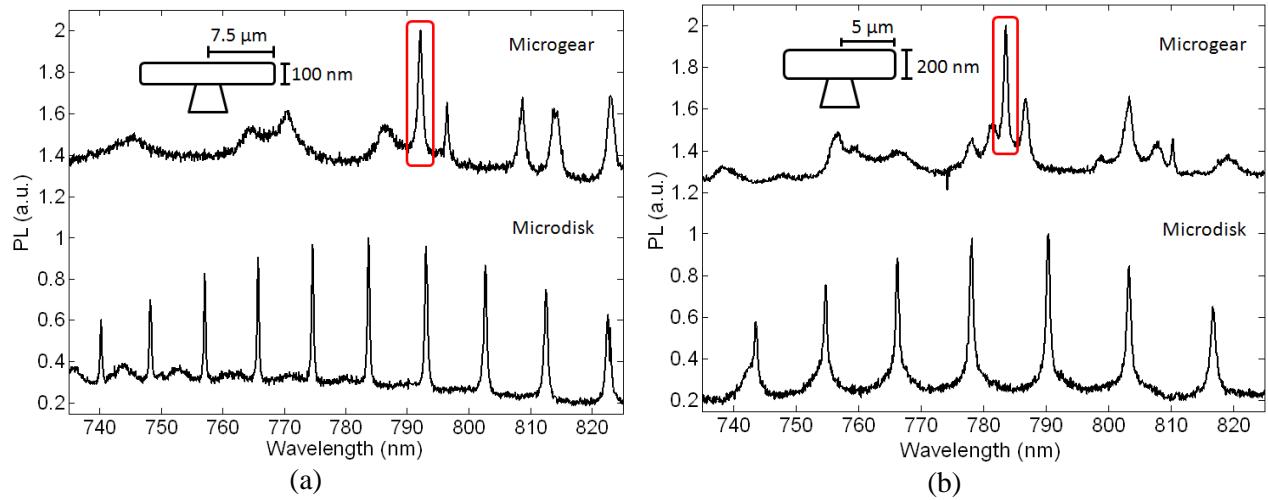


**Figure 31.** (a) PL collected from a 100 nm thick, 7.5  $\mu\text{m}$  radius Si-nc microgear and reference microdisk. (b) PL spectra collected from a 200 nm thick, 5  $\mu\text{m}$  radius Si-nc microgear and reference microdisk. The selected microgear mode in each case is indicated by a red box. After [23].

In this report, we have presented the salient results from our investigation of quantum confined Si films. We developed and optimized a Si-nc fabrication process and performed extensive material characterization. We demonstrated EL, investigated the carrier transport mechanism, and developed a pulsed pumping scheme to increase the material efficiency and stability. We then developed a device level modeling tool which accounted for the unique emission and gain behavior of Si-nc films by coupling a rate equation model with Maxwell's equations within the ADE-FDTD framework. We applied this modeling tool to design a series of Si-nc based devices for enhanced spontaneous emission and amplification. Based on these

designs, we fabricated a series of active Si-nc based photonic devices. Experimentally, we observed enhanced photo- and electro-luminescence in vertically emitting DBR microcavities. We also fabricated Si-nc microdisks and confirmed the existence of WGMs in the Si-nc PL spectrum with quality factors as high as  $2 \times 10^3$ , limited by the resolution of our spectrometer. We then designed a concentric microdisk structure consisting of an inner Si-nc disk and an outer Er:SiO<sub>2</sub> ring in order to convert the Si-nc emission to  $\sim 1500$  nm. We experimentally demonstrated excitation of higher order radial WGMs in the Si-nc luminescence spectrum and first order radial WGMs in the erbium emission spectrum. Finally, we performed the first investigation of microgear resonators applied to the Si-nc material system. We fabricated microgears with a range of gear teeth geometry and number of gear teeth and observed a single dominant mode in the PL spectrum. We demonstrated the ability to tune the emission wavelength by varying the number of gear teeth and also demonstrated methods to increase the quality factor by decreasing the radiative bending loss. This work represents a significant step in understanding the Si-nc material system and its applicability in light emitting photonic devices.

## 4.2 Quantum confinement for an enhanced electro-optic effect

The realization of a III-V compatible material with non-linear optical susceptibility on par with or greater than leading electro-optic (EO) materials, such as LiNbO<sub>3</sub>, would provide a key solution to the high speed optical modulation demands of numerous applications including mmW imaging. The strength of the second order nonlinear optical susceptibility determines a material's linear electro-optic coefficient, exploited in optical modulator designs for its fast response. The second order susceptibility only exists in non-centrosymmetric materials such as III-Vs. Unfortunately, the coefficient in bulk III-Vs is still an order of magnitude weaker than that in leading EO materials. Quantum dots fabricated in III-V materials (In/Al/GaAs) have demonstrated electro-optic coefficients orders of magnitude stronger than their bulk counterparts [25, 26]. Unfortunately, the molecular beam epitaxy (MBE) processes necessary to grow these dots induce limitations on the density of dots and the asymmetry which is thought to play a crucial role in the enhanced nonlinearity. Using selective etching techniques which will be discussed in the next section it may be possible to achieve high densities of quantum dot like III-V structures with increased asymmetry. In this section we present modeling using *ab initio* techniques to understand the role of the dot geometry on the nonlinear optical susceptibility and identify geometries which could further exploit this phenomena.

The nonlinear optical susceptibility of a material can be extracted by studying the dependence of polarization on electric field. We employ Density Functional Theory (DFT) to study this dependence in quantum confined systems with varying geometry. DFT solves for the ground state of a given system as a function of electron density. In this case, we first solve for the ground state of a system consisting of a single electron within a two-dimensional potential well of some geometry. We then apply an external electric field and solve for the ground state in this new configuration. By monitoring the macroscopic polarization of the system under perturbations of the electric field we are able to extract a term representing the quadratic dependence. This quadratic term  $\beta$ , similar to  $\chi^{(2)}$ , acts as a metric when comparing possible the enhanced EO in varying geometries.

### 4.2.1 Modeling the quantum confinement effect on the non-linear optical susceptibility

To demonstrate this approach, we first consider a two-dimensional, triangular potential. The triangle shape is defined by the ratio of its height to its base. The base is set to 1nm for all geometries. A single electron is introduced within this potential. Fig. 32 shows the electron density without an electric field and with fields applied in opposite directions. The asymmetric effect of an electric field on the density is evident.

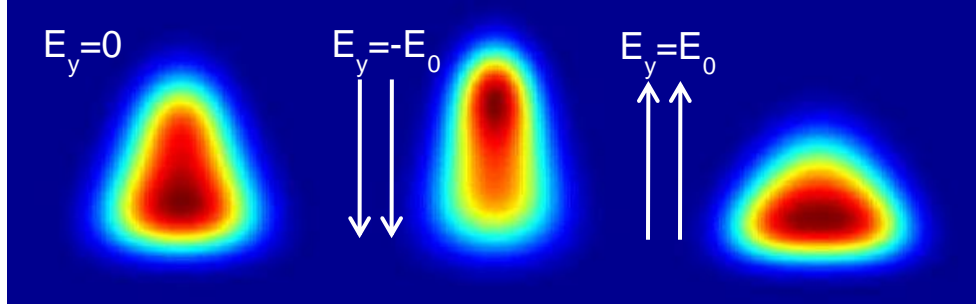


**Figure 32.** Electron density in a triangular potential with and without an external electric field.

The polarization is then plotted as a function of electric field. The polarization saturates for strong electric fields due to the infinite potential barrier at the boundaries of the triangle. However, in the region of small perturbations to the electric field, a quadratic dependence is observed, denoted here as  $\beta$ . This dependence is shown in Fig. 33(a). The  $\beta$  term is then extracted for triangles with aspect ratios ranging from 0.25 to 2.5, as shown in Fig. 33(b). The observed peak in the magnitude of  $\beta$  allows us to identify an optimal triangular geometry as having an aspect ratio between 1.5 and 1.75. A material with a triangular potential corresponding to this aspect ratio should exhibit the strongest nonlinear optic susceptibility, for this simplified study.

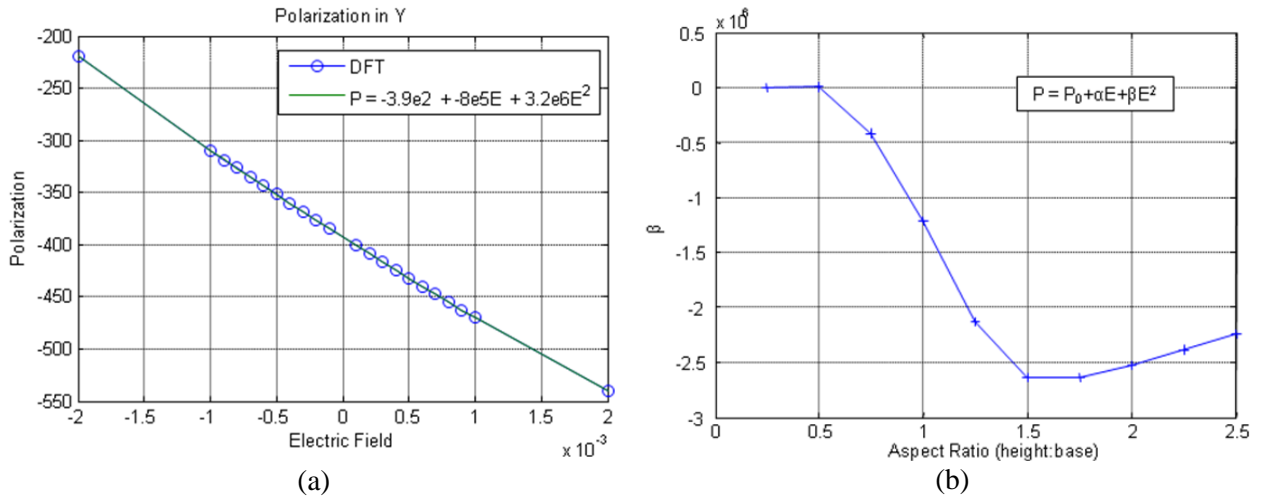
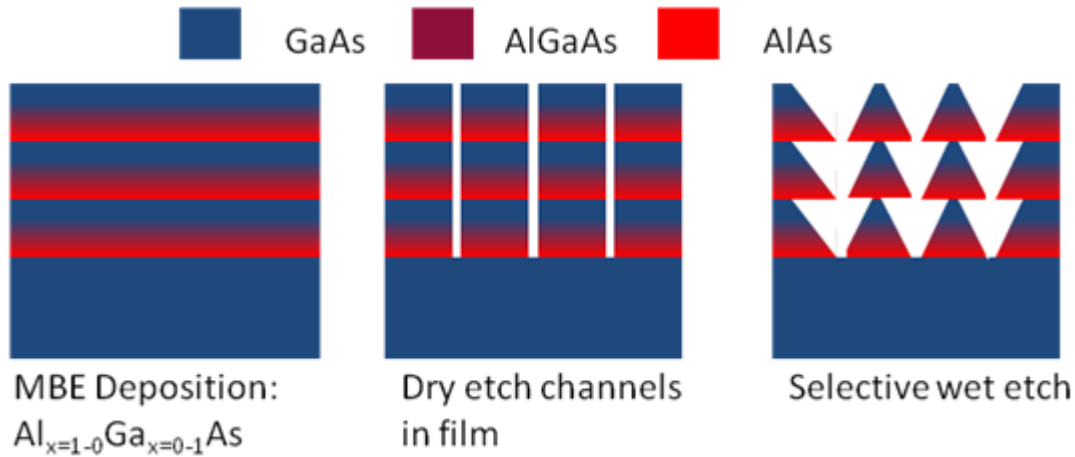


**Figure 33.** (a) Polarization for a triangular potential under perturbations to the electric field, as computed by DFT, and a polynomial fit yielding a quadratic term,  $\beta$ . (b)  $\beta$  for triangles with varying aspect ratios. An optimal geometry is identified as having an aspect ratio between 1.5 and 1.75.

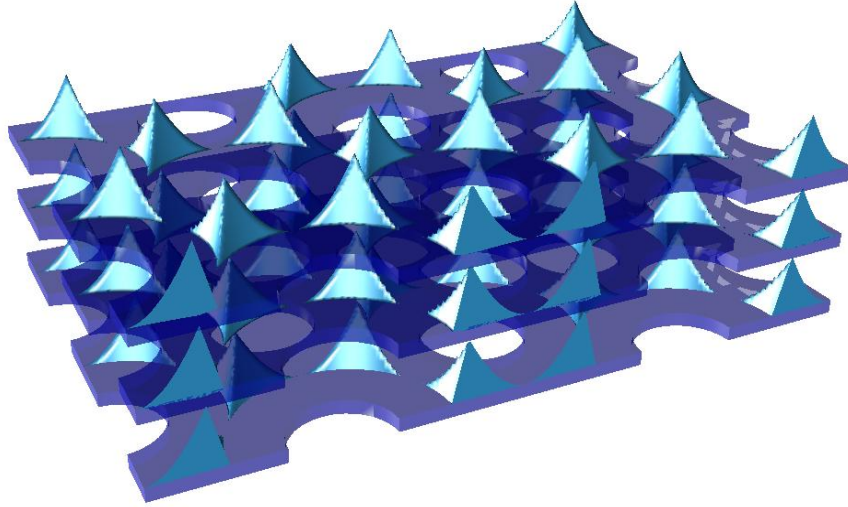
In the future, we plan to tailor these simulations to the III-V material of interest (likely GaAs or AlGaAs) by incorporating the effective mass and dielectric constants of the host material. We will also consider extending the simulation to a 3D geometry where we can study the varying effects of conical vs. pyramidal shaped potentials.

#### 4.2.2 Fabrication of QD type materials with selective etching etc

To realize the quantum confined structures modeled in the previous section we are developing a fabrication process based on a wet etching technique with high selectivity based on the Al concentration in AlGaAs films [27]. Preliminary calibration has demonstrated that a 4:1 ratio of citric acid to hydrogen peroxide etches GaAs at a rate approximately 100 times faster than  $\text{Al}_{0.3}\text{Ga}_{0.7}\text{As}$ . To take advantage of this effect, we propose a material based on an MBE grown film of AlGaAs with varying concentration throughout its thickness. By lithographically patterning holes on the film and dry etching channels, we access the various levels of  $\text{Al}_x\text{Ga}_{1-x}\text{As}$  with the wet etching solution. The proposed fabrication process is shown schematically in Figure 34.



(a)



(b)

**Figure 34.** (a) Proposed fabrication process for realization of high density quantum confined AlGaAs with arbitrary aspect ratio. (b) 3D rendering of proposed quantum confined structure.

We prepared a calibration sample with MBE layers of varying Al concentration as shown in Fig. 35(a). Straight lines were patterned on the surface and ICP etching opened channels for the wet etch. Cross sectional SEM images before and after the wet etch are shown in Figure 35(b). The wet etchant clearly distinguishes between GaAs and AlGaAs, and the AlGaAs layer with 10% Al etches at a slower rate than GaAs. Layers with an Al concentration of 20% or higher were not measurably etched. Further calibration will focus on layers with Al concentration between 0 and 20%.

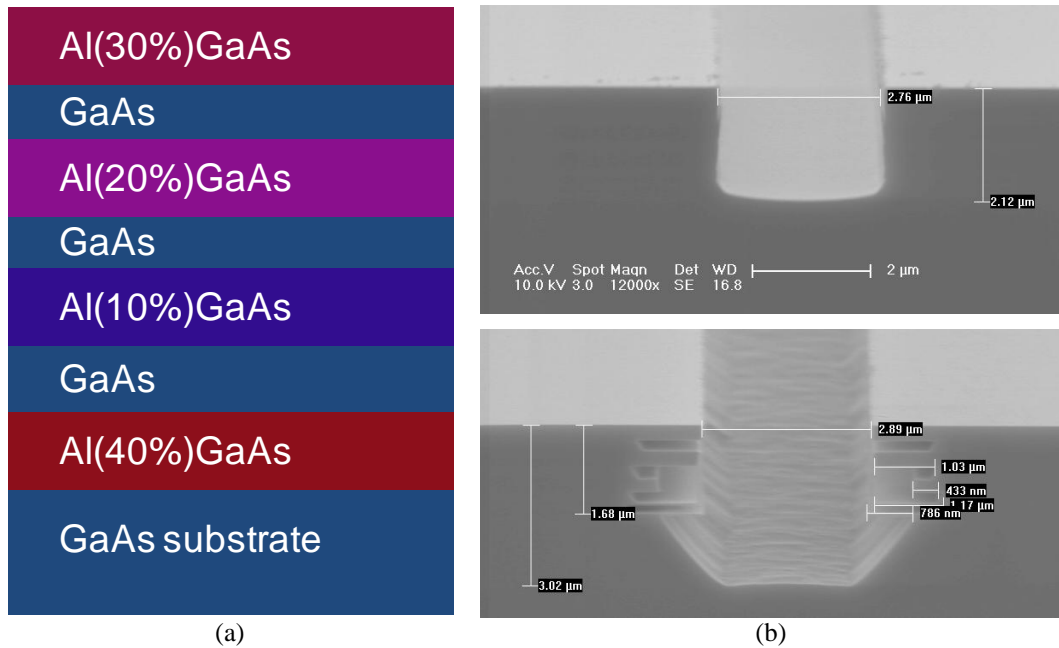


**Figure 35.** (a) Schematic of Al Concentration in MBE AlGaAs film. (b) Cross sectional SEM image of AlGaAs after dry etching (top) and subsequent selective wet etch

(bottom). The AlGaAs etch rate is reduced with increasing Al concentration.

This method promises to allow for precise control of the size and shape of the quantum confined AlGaAs material. Furthermore, we no longer need to compensate for strain, as in typical self assembled quantum dot growth, allowing us to achieve a very high density of quantum confined material.

## 5 Personnel Supported

**Faculty** : Prof. Dennis Prather  
**Post Doctorate:** Ahmed Sharkawy (10%)  
**Graduate students:** Brandon Redding, Tim Creazzo, Xi Long

## 6 Publications

1. B. Redding, S. Shi, T. Creazzo, D. W. Prather, "Electromagnetic modeling of active silicon nanocrystal waveguides," *Optics Express* **16**, 8792 (2008).
2. S. Shi, B. Redding, T. Creazzo, E. Marchena, D. W. Prather, "Quantum Electrodynamics Modeling of Silicon-Based Active Devices," *Advances in Optical Technologies* **2008**, 615393 (2008).
3. E. Marchena, S. Shi, D. W. Prather, "Fabrication and characterization of optimized corner-cut square microresonators," *Optics Express*, **16**, 16516 (2008).
4. B. Redding, T. Creazzo, E. Marchena, S. Shi, D. W. Prather, "Coupling Si Nanocrystal Microdisk Emission to Whispering Gallery Modes in a Concentric SiO<sub>2</sub> Ring," *Optics Letters* **34**, 1384 (2009).
5. B. Redding, S. Shi, D. W. Prather, "Electromagnetic Analysis of Ring Cavity Assisted Amplified Spontaneous Emission in Er: SiO<sub>2</sub>/a-Si Horizontal Slot Waveguides," *IEEE Journal of Quantum Electronics* **45**, 825 (2009).
6. S. Shi, B. Redding, T. Creazzo, E. Marchena, D. W. Prather, "Modeling of light amplification and enhanced spontaneous emission in silicon nanocrystals," *Journal of Nanophotonics* **3**, 033503 (2009).
7. D. W. Prather, B. Redding, T. Creazzo, E. Marchena, S. Shi, "Integration of Silicon Nanocrystals and Erbium Ring Cavities for a Silicon Pumped Er:SiO<sub>2</sub> Laser," *Journal of Nanoscience and Nanotechnology* **10**, 1 (2010).
8. T. Creazzo, B. Redding, E. Marchena, J. Murakowski, D. W. Prather, "Tunable Photoluminescence and Electroluminescence of Size-controlled Silicon Nanocrystals in a-Si/SiO<sub>2</sub> Superlattices," *Journal of Luminescence* **130**, 631 (2010).
9. E. Marchena, B. Redding, T. Creazzo, S. Shi, D. W. Prather, "Whispering gallery modes at 800 nm and 1550 nm in concentric Si-nc/Er:SiO<sub>2</sub> microdisks," *Journal of Nanophotonics* **4**, 049501 (2010).
10. B. Redding, E. Marchena, T. Creazzo, S. Shi, D. W. Prather, "Comparison of raised microdisk whispering gallery mode characterization techniques," *Optics Letters* **35**, 998 (2010).

11. T. Creazzo, B. Redding, E. Marchena, R. Hao, J. Murakowski, S. Shi, and D. W. Prather, "Distributed Bragg Reflector Enhancement of Electroluminescence from a Silicon Nanocrystal Light Emitting Device," *Thin Solid Films* **518**, 4394 (2010).
12. T. Creazzo, B. Redding, E. Marchena, J. Murakowski, and D. W. Prather, "Pulsed Pumping of Silicon Nanocrystal Light Emitting Devices," *Optics Express* **18**, 10924 (2010).
13. B. Redding, S. Shi, T. Creazzo, E. Marchena, D. W. Prather, "Design and Characterization of Silicon Nanocrystal Microgears," *Photonics and Nanostructures* (In press).
14. E. Marchena, B. Redding, T. Creazzo, D. W. Prather, "Mitigation of Si nanocrystal free carrier absorption loss at 1.5  $\mu\text{m}$  in a concentric microdisk structures," *Optics Letters* (In review).

## **7 Interactions/Transitions**

None

## **8 New Discoveries**

None

## **9 Honors/Awards**

None

## **10 References**

- [1] F. Iacona, G. Franzo and C. Spinella. *Journal of Applied Physics*, **87**, 1295 (2000).
- [2] T. Creazzo, B. Redding, E. Marchena, J. Murakowski and D. W. Prather. *Journal of Luminescence*, **130**, 631 (2009).
- [3] S. Shi, B. Redding, T. Creazzo, E. Marchena and D. W. Prather. *Advances in Optical Technologies*, **2008**, 615393 (11 pp.) (2008).
- [4] G. Franzo, A. Irrera, E. C. Moreira, M. Miritello, F. Iacona, D. Sanfilippo, G. Di Stefano, P. G. Fallica and F. Priolo. *Applied Physics A: Materials Science and Processing*, **74**, 1 (2002).
- [5] X. D. Pi, O. H. Y. Zalloum, A. P. Knights, P. Mascher and P. J. Simpson. *Journal of Physics Condensed Matter*, **18**, 9943 (2006).
- [6] W. R. Harrell and J. Frey. *Thin Solid Films*, **352**, 195 (1999).
- [7] S. M. Sze and K. K. Ng. in *Physics of Semiconductor Devices*, Wiley, Hoboken (2007).
- [8] A. Irrera, F. Iacona, I. Crupi, C. D. Presti, G. Franzo, C. Bongiorno, D. Sanfilippo, G. Di Stefano, A. Piana, P. G. Fallica, A. Canino and F. Priolo. *Nanotechnology*, **17**, 1428 (2006).
- [9] A. Marconi, A. Anopchenko, M. Wang, G. Pucker, P. Bellutti and L. Pavesi. *Applied Physics Letters*, **94**(2009).

- [10] R. J. Walters, G. I. Bourianoff and H. A. Atwater. *Nature Materials*, **4**, 143 (2005).
- [11] J. Barreto, M. Peralvarez, J. A. Rodriguez, A. Morales, M. Riera, M. Lopez, B. Garrido, L. Lechuga and C. Dominguez. *Physica E*, **38**, 193 (2007).
- [12] T. Creazzo, B. Redding, E. Marchena, J. Murakowski and D. W. Prather. *Optics Express*, **18**, 10924 (2010).
- [13] A. S. Nagra and R. A. York. *IEEE Transactions on Antennas and Propagation*, **46**, 334 (1998).
- [14] L. Dal Negro, M. Cazzanelli, N. Daldosso, Z. Gaburro, L. Pavesi, F. Priolo, D. Pacifici, G. Franzo and F. Iacona. *Physica E: Low-Dimensional Systems and Nanostructures*, **16**, 297 (2003).
- [15] B. Redding, S. Shi, T. Creazzo and D. W. Prather. *Optics Express*, **16**, 8792 (2008).
- [16] B. Redding, E. Marchena, T. Creazzo, S. Shi and D. W. Prather. *Optics Letters*, **35**, 998 (2010).
- [17] D. Navarro-Urrios, A. Pitanti, N. Daldosso, F. Goubilleau, L. Khomenkova, R. Rizk and L. Pavesi. *Physica E: Low-Dimensional Systems and Nanostructures*, **41**, 1029 (2009).
- [18] R. D. Kekatpure and M. L. Brongersma. *Optics Letters*, **34**, 3397 (2009).
- [19] D. W. Prather, B. Redding, T. Creazzo, E. Marchena and S. Shi. *Journal of Nanoscience and Nanotechnology*, **10**, 1-7 (2010).
- [20] B. Min, T. J. Kippenberg, L. Yang, K. J. Vahala, J. Kalkman and A. Polman. *Physical Review A - Atomic, Molecular, and Optical Physics*, **70**, 033803 (2004).
- [21] B. Redding, T. Creazzo, E. Marchena, S. Shi and D. W. Prather. *Optics Letters*, **34**, 1384 (2009).
- [22] E. Marchena, B. Redding, T. Creazzo, S. Shi and D. W. Prather. *Journal of Nanophotonics*, **4**, 049501 (2010).
- [23] B. Redding, S. Shi, T. Creazzo, E. Marchena and D. W. Prather. *Photonics & Nanostructures*, ((Accepted)).
- [24] K. P. Huy, A. Morand and P. Benech. *IEEE Journal of Quantum Electronics*, **41**, 357 (2005).
- [25] S. Ghosh, A. S. Lenihan, M. V. G. Dutt, O. Qasaimeh, D. G. Steel and P. Bhattacharya. *Journal of Vacuum Science & Technology B (Microelectronics and Nanometer Structures)*, **19**, 1455 (2001).
- [26] J. Tatebayashi, R. B. Laghumavarapu, N. Nuntawong and D. L. Huffaker. *Electronics Letters*, **43**, 410 (2007).
- [27] G. C. DeSalvo, W. F. Tseng and J. Comas. *Journal of the Electrochemical Society*, **139**, 831 (1992).